



HAL
open science

Raman spectroscopy investigations of the Martian regolith breccia Northwest Africa 7533: A support to in situ Raman spectroscopy on Mars

Virgile Malarewicz, Brigitte Zanda, Olivier Beyssac, Roger Hewins, Sylvain Pont, Sylvain Bouley, Sylvain Bernard, Michel Gauthier, Marc Morand, Yiuri Garino, et al.

► To cite this version:

Virgile Malarewicz, Brigitte Zanda, Olivier Beyssac, Roger Hewins, Sylvain Pont, et al.. Raman spectroscopy investigations of the Martian regolith breccia Northwest Africa 7533: A support to in situ Raman spectroscopy on Mars. *Journal of Raman Spectroscopy*, 2023, 54 (7), pp.748-768. 10.1002/jrs.6556 . hal-04196547

HAL Id: hal-04196547

<https://hal.science/hal-04196547>

Submitted on 11 Oct 2023

HAL is a multi-disciplinary open access archive for the deposit and dissemination of scientific research documents, whether they are published or not. The documents may come from teaching and research institutions in France or abroad, or from public or private research centers.

L'archive ouverte pluridisciplinaire **HAL**, est destinée au dépôt et à la diffusion de documents scientifiques de niveau recherche, publiés ou non, émanant des établissements d'enseignement et de recherche français ou étrangers, des laboratoires publics ou privés.

Raman spectroscopy investigations of the Martian regolith breccia Northwest Africa 7533: A support to *in situ* Raman spectroscopy on Mars

Likely to be submitted to Journal of Raman Spectroscopy.

Authors

Malarewicz, Zanda, Beyssac, Hewins, Pont, Bouley, Bernard, Gauthier, Morand, Garino, Rosier.

Abstract

Using continuous-wave and time-resolved Raman spectroscopy, we investigate and characterize main and minerals of NWA 7533, a unique Martian regolith breccia. This regolith breccia is a crucial sample, giving unique access to the formation and evolution of the primitive Martian crust, with crystallization processes beginning up to ~4.4 Ga years ago. We provide an overview of Raman spectra for feldspar, plagioclase, pyroxene, olivine, apatite, merrillite, zircon, pyrite, and various Fe-Cr-Ti oxides like magnetite, hematite, ilmenite and rutile. Most analytical points are paired with previous electron microprobe analyses by Hewins et al. (2017) for deeper interpretation of Raman data. Composition variation of the silicate minerals obtained through microanalysis is traced through variation of the Raman peak characteristics. No trace of any shock event is observed in the mineral structures. Structural diversity of zircon is linked to various metamictization stages. The luminescence signal of REE-bearing minerals, mainly phosphate and zircon, is documented in detail and discussed. Using all these data, we discuss the presence of at least two generations of phosphate minerals with implications for magmatic petrology.

1/ Introduction

Raman spectroscopy has been carried out on Mars since the NASA Perseverance rover landing on February 18th 2021 at Jezero Crater. Perseverance actually carries a sophisticated payload of scientific instruments to conduct *in situ* geological investigations and characterize the environment of samples collected for return to Earth in the future by the NASA-ESA Mars Sample Return (MSR) program (Farley et al., 2022). The presence of Raman on Mars constitutes a strong recognition for this technique now commonly used in mineralogy laboratories (e.g., Pasteris and Beyssac, 2020). In fact, this is somewhat overdue on Mars, as a scheduled Raman instrument was removed from the scientific payload of the now legendary Mars Exploration rovers Spirit and Opportunity in 2004. There are two complementary instruments using Raman spectroscopy aboard Perseverance which are called SuperCam and SHERLOC. The SuperCam instrument combines multiple investigation techniques: Laser Induced Breakdown Spectroscopy (LIBS), Time-Resolved Raman (TRR) and Luminescence (TRL) spectroscopy in addition to Visible (VIS) and infrared (IR) spectroscopy, a microphone and a

remote micro-imager (RMI). This versatile remote-sensing instrument provides chemical and mineralogical information from the same spot on the target at a sub-millimetric to millimetric scale (Maurice et al., 2021; Wiens et al., 2021). To do this, SuperCam is composed of a mast unit on top of the Perseverance mast and a body unit within the rover belly connected by an optical fiber. The second instrument is SHERLOC which is a deep-UV Raman spectrometer optimized to detect, analyze, and map the distribution of organics in the targeted rock (Bhartia et al., 2021), but it can also perform Raman spectroscopy on some minerals. The SHERLOC instrument is combined with a high-resolution, context imager called Watson. Both instruments are performing well on Mars and have already provided key observations (Scheller et al., 2022; Wiens et al., 2022). In addition, a third Raman instrument should be deployed on Mars in the near future: the RLS (Raman Laser Spectrometer) instrument onboard the ESA Rosalind Franklin rover (Rull et al., 2017). This mission has known many delays and postponements of the launch, the last one being due to the interruption of ESA-Roscosmos collaboration after the invasion of Ukraine in 2022. RLS is more conventional as it is a continuous-wave Raman spectrometer operating in a microscopy configuration bearing similarities with laboratory commercial Raman spectrometers (Rull et al. 2017). Last, an instrument with a similar configuration will be aboard the rover deployed by the JAXA MMX mission on Phobos, the main moon of Mars (Cho et al., 2021). Interpretation of remote Raman spectroscopic observations may be greatly aided by laboratory study of similar materials.

In recent years, Martian geology has been revolutionized by the discovery of a primitive differentiated Martian crust based on mineralogical observations from orbit, *in situ* and from meteorites. Until recently, the surface of Mars was generally considered as a monotonous basaltic world with local alteration features mostly due to hydrothermal activity. Recent findings and observations have actually challenged this idea revealing a more complex chemical and lithological pattern for the oldest widespread terranes from the Noachian period. First, a unique meteorite *Black Beauty* (NWA 7533, NWA 7034 and paired meteorites) was recently discovered and is interpreted as a Martian regolith breccia (Humayun et al., 2013). While the classical Martian meteorites (SNCs for Shergottite, Nakhilite, Chassignite) sample deeper mantle-derived rocks or basaltic fractions of Mars, *Black Beauty* represents a unique sampling of Mars' surface. This breccia actually includes an extraordinary diversity of lithic clasts in a microcrystalline matrix. These clasts represent various stages of geochemical differentiation from basalts to monzonitic compositions through melt rocks (Hewins et al., 2017; McCubbin et al., 2016; Santos et al., 2015; Wittmann et al., 2015). Timing of the complex history for this peculiar meteorite is well established by geochronology and, interestingly, most of the clasts are dated from the earliest era of Mars history, the Pre-Noachian era (Humayun et al., 2013). This meteorite thus provides a unique window on the early Mars surface. In the meantime, the NASA rover MSL Curiosity has made fundamental discoveries *in situ* in Gale crater on Mars since 2013. Using the onboard instruments including the ChemCam LIBS, Sautter et al. (2015) found some

felsic rocks with highly differentiated mineralogical and average chemical compositions ranging from alkali basalts to trachyte. Last, some occurrences of differentiated feldspar- and silica-rich rocks were detected from orbit by infrared spectrometers aboard orbiters (Carter and Poulet, 2013; Rogers and Nekvasil, 2015).

Altogether, looking at this single rock (NWA7533) offers a unique opportunity to analyze the mineralogy of many contrasted lithologies that are present on the surface of Mars and that could be encountered by rovers. Interestingly, some of the clasts come from the primitive Martian crust, not only offering an access to the geodynamical processes on early Mars, but also to the period when Mars has possibly hosted life on its surface. In this article, we investigate several sections of NWA7533 by Raman spectroscopy covering all the mineral phases documented so far for this unique meteorite. For this, we use both continuous-wave and time-resolved Raman spectroscopy using analytical configurations similar to some of the Raman instruments sent on Mars. We explore Raman spectra and Raman peak characteristics of all minerals present, some combined with previous chemical analysis using electron microprobe (EMP) and scanning electron microscopy (SEM) (Hewins et al. 2017). Raman spectroscopy also allows us to investigate luminescence signals from Rare-Earth Elements (REE) present as trace elements in accessory minerals, such as zircon and apatite. Such trace elements are useful tracers for geochemical processes and are widely used in geochronology so any *in situ* detection on Mars would be of important scientific interest. The data base we present here will be useful in future interpretation of rover spectroscopic observations.

2/ *Black Beauty*: NWA7533, NWA7034 and paired meteorites

Recovered in the Sahara Desert in the early 2010s, NWA 7533 and paired NWA 7034 are the first identified breccia of Martian origin identified by isotopic values (Agee et al., 2013) and trapped noble gas content (Cartwright et al., 2014). The bulk composition of NWA 7533 is similar to alkali basalt (Hewins et al. 2017), but it displays a highly complex structure including strong variability of lithic clasts, and thus cannot be directly related to the classical series of Martian SNC meteorites. In addition, dating zircons and other accessory minerals revealed primary crystallization processes around 4.4 Ga, making some clasts the oldest known Martian rocks. Remarkably, this regolith breccia contains a wide diversity of lithic clasts, from fragments of microbasalts to fragments of mafic *plutonic* rocks with noritic or monzonitic bulk composition. It also contains crystal clasts and partial lithic clasts with various mineral phases, like feldspars, from plagioclase to alkali composition, and pyroxenes with composition varying from augite, pigeonite to orthopyroxenes. The meteorite also contains impact melt spherules and Clast-Laden Melt Rocks (CLMR). All these constitutive objects are embedded in a very fine-grained crystalline matrix. The matrix is composed of micron-sized

plagioclase, feldspar and pyroxene, intimately mixed with Fe-rich micro-phases like various Fe-Ti-Cr oxides or sulfides, mainly magnetite and pyrite.

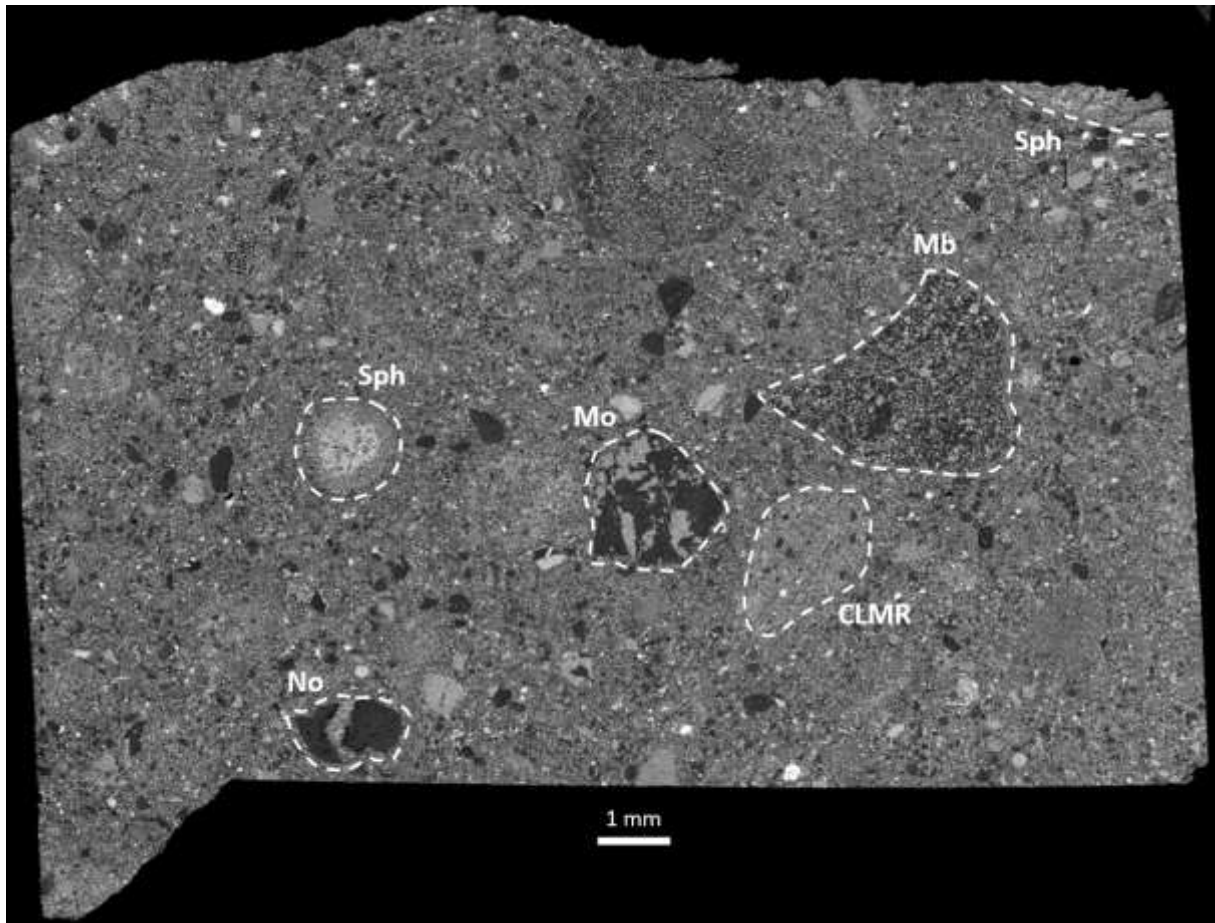


Fig.1 : Back-scattered Electron (BSE) image obtained by SEM from the NWA7533 section SP6. Several clasts are highlighted by Mb (Microbasalts), Sph (Spherules), Mo (Monzonitic clasts), No (Noritic clasts) and CLMR (Clast Laden Melt Rocks).

In this study, several polished sections of NWA7533 were studied. Figure 1 depicts a global image of section SP6 of NWA 7533 and shows the diversity of lithic clasts as well as the highly complex texture of this rock. Basaltic and microbasaltic clasts are common in all sections of NWA 7533, with granoblastic or subophitic textures and grain size generally ranging between $\sim 50 \mu\text{m}$ and $\sim 100 \mu\text{m}$. These clasts are made of pyroxenes, with augite-pigeonite composition, plagioclase, rarely K-feldspar, Fe-oxide minerals, phosphates and small zircons. These clasts have a bulk chemical composition and mineral assemblage globally similar to that of SNC meteorites. Some other igneous clasts have generally larger grain size ($> 200 \mu\text{m}$) and exhibit noritic or monzonitic compositions. Noritic clasts are usually composed of feldspar plagioclase, orthopyroxene and pigeonite, with Cr-Ti magnetite. Monzonitic clasts are generally composed by alkali feldspar, plagioclase, augite, Ti-magnetite, chloroapatite and zircons (Hewins et al. 2017). The bulk composition of some of these clasts is highly differentiated in the alkaline series in a TAS diagram. The composition of these clasts

converge towards compositions of some rocks analyzed *in situ* at Gale crater by NASA MSL Curiosity rover (Sautter et al., 2015). Along, with a marked enrichment in incompatible elements (Humayun et al., 2013; Hewins et al. 2017), the presence of monzonitic clasts in the breccia suggests that a differentiated crust had rapidly formed in Mars history.

Because of siderophile element abundances, most objects found in the breccia except magnesian orthopyroxene clasts were interpreted as impact-related, like impact melt spherules and Clast Laden Melt Rocks (CLMR). Spherules are amongst the biggest objects found in the breccia, locally exceeding 5 mm in diameter, making them easily recognized by the naked eye. Their textural habit may be vitrophyric or crystalline, often filled with fine-grained crystalline pyroxene and feldspath (1-5 μm). Some Fe- and Cr- rich oxides are locally observed as well as one occurrence of long chains of dendritic olivines. CLMR can be a dominant component in some sections of NWA 7533, with varying aerodynamical shapes and a subophitic plagioclase-pyroxene matrix containing clusters of pyroxenes, associated with various oxides, often surrounded by overgrown fine-grained plagioclase. This is the result of transported partially molten materials accumulating all sorts of debris along the way.

3/ A brief presentation of the Raman systems presently on or going to Mars

SHERLOC aboard Perseverance is an instrument for proximity Science, i.e. working at the contact of rocks, using a deep UV Raman spectrometer with a laser at 248.6 nm focused on a spot of $\sim 100 \mu\text{m}$ on the sample surface (Bhartia et al. 2021). SHERLOC can do rasters on the sample and is combined with PIXL, an X-ray fluorescence-based instrument, for chemistry. SHERLOC is overall optimized to excite and analyse fluorescence and Raman signals from organic compounds. The key advantage here is that UV is highly efficient to excite fluorescence and that the Raman spectral window is shifted and free of luminescence/fluorescence signal (Beysac, 2022; Bhartia et al., 2021). The disadvantage is that deep UV light imposes severe restrictions in terms of instrumental design including the cutoff of the signal at about 800 cm^{-1} limiting the possible characterization of many silicate minerals. First detections reported by Sherloc at Jezero crater include carbonates, sulfates, perchlorates, phosphates and olivine (Scheller et al., 2022).

SuperCam Raman is a remote-sensing instrument which analyses the chemistry and mineralogy of targets less than a few meters from the rover: it is the eye of the rover. SuperCam Raman uses nanosecond pulsed laser at 532 nm which is collimated on the surface of the target. By means of a Schmidt-Cassegrain telescope, light emitted from the laser spot is collected and sent by an optical fiber to the spectrometer. The latter is an original transmission spectrometer dispersing light towards a gated Intensified CCD. SuperCam uses time-resolved Raman and luminescence spectroscopy to reject daylight entering the telescope and to explore both phenomena in the time-domain (Beysac, 2020). Vibrational transitions involved in the Raman effect are nearly immediate

with extremely short lifetime ($<10^{-14}$ seconds) and will last only during the laser pulse. The electronic transitions involved in luminescence have much longer lifetime, generally higher than the nanosecond, and therefore will continue long after the laser pulse. For time-resolved spectroscopy, the laser pulse is synchronized in the time-domain with the ICCD. To optimize the Raman signal, one will use a short gate for the ICCD matching precisely the laser pulse to reject most luminescence. Alternatively, opening the gate right after the laser pulse will reject the Raman signal and allows collection of Raman-free luminescence spectra. By using an appropriate combination of delays (time between the laser pulse and the opening of the gate) and gate duration, one may even get specific luminescence spectra for each activator. This is not possible with continuous-wave Raman spectroscopy which integrates all Raman and luminescence signals. Another characteristic of SuperCam Raman is the large size of the analytical footprint (0.75 mrad) which varies from 1.5 mm in diameter at 2 m to 3 mm at 4 m and higher values at larger distances. This implies that SuperCam Raman in general analyses mixtures of grains depending on the target grain size. SuperCam Raman analyses the raw surface of rocks, generally after LIBS for dust removal, or abraded patches on selected targets. First detections reported by SuperCam Raman at Jezero crater include carbonates, perchlorates and olivine (Wiens et al., 2022).

The RLS spectrometer has a more conventional design bearing similarities with commercial Raman microspectrometers, although it has been adapted, ‘spatialized’ in terms of weight, size, resistance, to fit the extremely heavy constraints driving the building of any space instrument (Rull et al., 2017). RLS uses a continuous-wave laser at 532 nm which is focused on a ~ 50 μm spot on the surface of the target using an objective. The same objective collects the signal emitted and sends it to a Czerny-Turner spectrometer and a CCD. The MMX Raman instrument has a design similar to the RLS instrument but will work directly on the raw surface of rocks below the rover (Cho et al., 2021).

4/ Methodology

4.1/ Continuous-wave Raman including hyperspectral mapping

All samples were analyzed using a continuous-wave Raman microspectrometer Renishaw InVia Reflex for point analyses and Raman hyperspectral mapping when needed. Measurements were performed using a green 532 nm solid-state laser focused on the sample through a Leica DM2500 microscope with short-working distance 50X or 100X objectives (NA = 0.85-0.90). This configuration yields a planar resolution of approximately 1-2 μm for a laser power of less than 1 mW delivered at the sample surface, using neutral density filters to prevent irreversible thermal damage (see Fau et al., 2019 for discussion). This corresponds to a laser irradiance in the range of 0.3 to 1.3 10^9 Wm^{-2} . All measurements were performed with a circularly polarized laser beam using a $\frac{1}{4}$ -wave plate placed before the microscope in order to minimize polarization effects. The Raman signal was dispersed by a grating with 2400 lines/mm and the signal was analyzed with a RENCAM CCD detector. The spectral

resolution for visible light was 1 to 1.9 cm^{-1} and the wavenumber accuracy was better than 0.5 cm^{-1} . The values of the full width at half-maximum (FWHM) of the Raman peaks were corrected considering the spectral resolution using the method described by Váczi, (2014). For Raman mapping and the acquisition of hyperspectral maps, the sample was moved with an appropriate step size using a XYZ Renishaw motorized stage. Laser focus was optimized by correcting topographic variation prior to analysis (surface mode using the Renishaw Wire 4.3 software) and all maps were processed using the Wire 4.3 software. Raman mapping is a powerful tool for deciphering the structural and textural variability within a single grain, or the phase identification and composition in a mineral assemblage. More details concerning the Raman mapping technique can be found in Bernard et al. (2008). All measurements were performed at room temperature and spectra were recorded directly from the raw samples without any preparation.

4.2/ Time-resolved Raman and luminescence spectroscopy

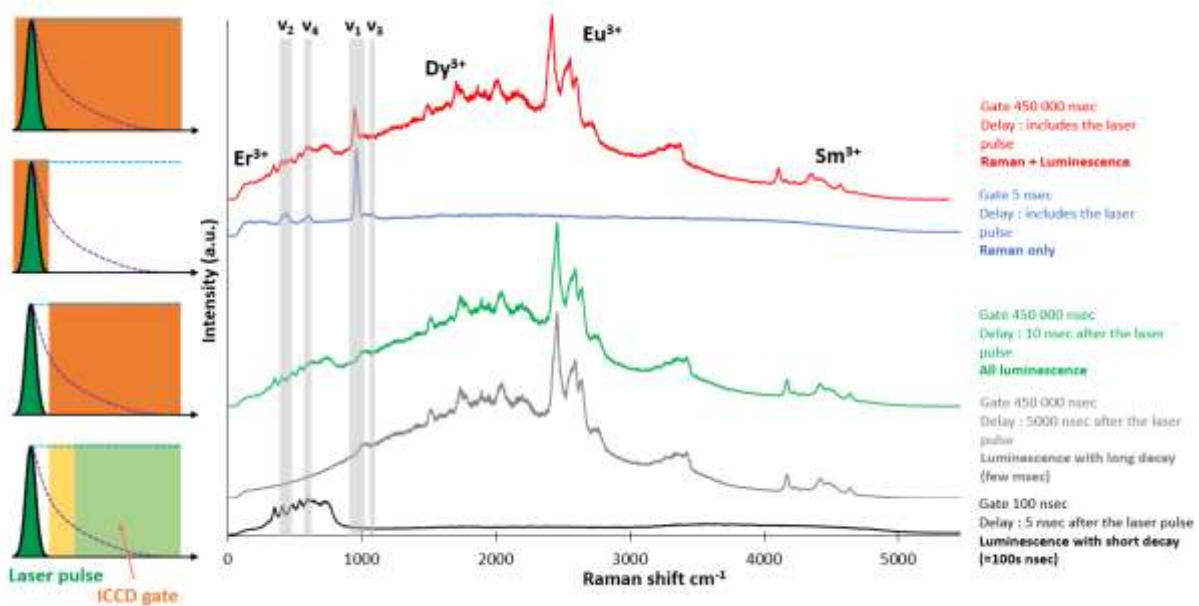


Fig. 2: Several time-resolved spectra on a merrillite grain illustrating the capability of time-resolved spectroscopy to separate Raman signal (Raman bands in grey) from the luminescence signals and to explore the luminescence signal (all, short- and long lived luminescence).

All samples were also analyzed using a custom-built, time-resolved Raman and luminescence spectrometer as described by (Fau et al., 2022, 2019). The laser is a nanosecond (1.2 ns FWHM, 1 mJ per pulse) pulsed, diode-pumped solid-state (DPSS) laser operating at 532 nm with a 10 to 2000 Hz repetition rate. The laser is slightly defocused at the sample surface through a microscope objective (MPlan Apo Mitutoyo 20X, NA= 0.42). The Raman and luminescence signals are collected using a backscattering geometry. In addition, the laser was circularly polarized with a $\frac{1}{4}$ -wave plate placed

before the microscope in order to minimize polarization effects. In this setup, a Notch filter cut off the Rayleigh scattering at $\sim 90 \text{ cm}^{-1}$. The signal was collected using an optical fiber and sent into a modified Czerny-Turner spectrometer (Princeton Instruments IsoPlane 320) coupled with an intensified Princeton Instruments PIMAX4 ICCD camera. The fine control of both the time delay and the gating time of the camera allows for sub-nanosecond time resolution experiments thanks to a precise synchronization between the laser pulse and the ICCD. This spectrometer has three motorized gratings, which can be selected depending on the spectral window and resolution required for the measurement. In this study, we mostly used a 600 lines/mm grating yielding a spectral resolution of $10\text{-}13 \text{ cm}^{-1}$ similar to the spectral resolution of SuperCam. Irradiance, associated with a pulsed laser, can be estimated as $Q/(\tau S)$, with $Q = P/f$ being the laser energy per pulse, P being the time-integrated laser power measured at the surface of the sample, f the laser repetition rate, τ the pulse duration, and S the surface area of the laser spot on the sample. For these experiments, irradiance was set at $\sim 10^{10} \text{ Wm}^{-2}$, which is a conservative value even in the case of absorbing minerals (Fau et al., 2019).

A non-polished section of the meteorite was also analyzed using a remote configuration described by Fau et al. (2019) and Megevand et al. (2021). In the remote setting, the laser is collimated at the sample surface 8 m from the telescope Schmidt plate on a spot of $\sim 6 \text{ mm}$ diameter, and the Raman signal is collected by a conventional Schmidt-Cassegrain telescope (Celestron-C8 202 mm diameter Schmidt plate) on a spot of $\sim 5 \text{ mm}$ diameter co-aligned with the laser spot. After the telescope, a notch filter cuts off the Rayleigh scattering at $\sim 90 \text{ cm}^{-1}$ and the signal is collected by an optical fiber and sent into the modified Czerny-Turner spectrometer coupled with the intensified ICCD camera.

4.3/ Continuous-wave (CW) versus time-resolved (TR) spectroscopy

Figure 2 shows a comparison of CW versus TR spectroscopy on a merrillite grain in NWA7533. This Ca-phosphate may include some REE during crystallization (see below) that will absorb the incident laser light and emit luminescence signal for relaxation. To keep the same analytical spot, CW spectroscopy is mimicked here by using a long ICCD gate of 450,000 ns and by opening the gate before the laser pulse: all Raman and luminescence signals are then included in the spectrum. The corresponding spectrum is dominated by the luminescence of various REE^{3+} hosted by the merrillite and only the main Raman peak (ν_1) of merrillite is clearly detected. Such complex spectra may be decomposed into a Raman spectrum and a luminescence spectrum. The Raman spectrum is obtained with a short ICCD gate of 5 ns and gate opening before the laser pulse while the total luminescence spectrum is obtained by using a long ICCD gate and opening just after the laser pulse. The luminescence signal may be then explored by using various combinations of gate delay and gate opening: short lifetime luminescence (e.g., Er^{3+}) is detected with a short gate just opened briefly after the pulse while long lifetime luminescence (e.g. Sm^{3+} , Eu^{3+}) is detected by opening a long gate

longer after the laser pulse. Another way to illustrate the capability of time-resolved spectroscopy to discriminate among various lifetime luminescences is to use a constant delay and increase the gate duration. Figure 3 shows luminescence spectra obtained on the same merrillite grain with a gate opening just after the laser pulse (no Raman) and increasing gate durations. Below 10000 ns, only the short lifetime luminescence of Er³⁺ is observed but several other luminescence peaks corresponding to longer lifetime luminescence (e.g. Sm³⁺, Eu³⁺) appear when increasing the gate duration.

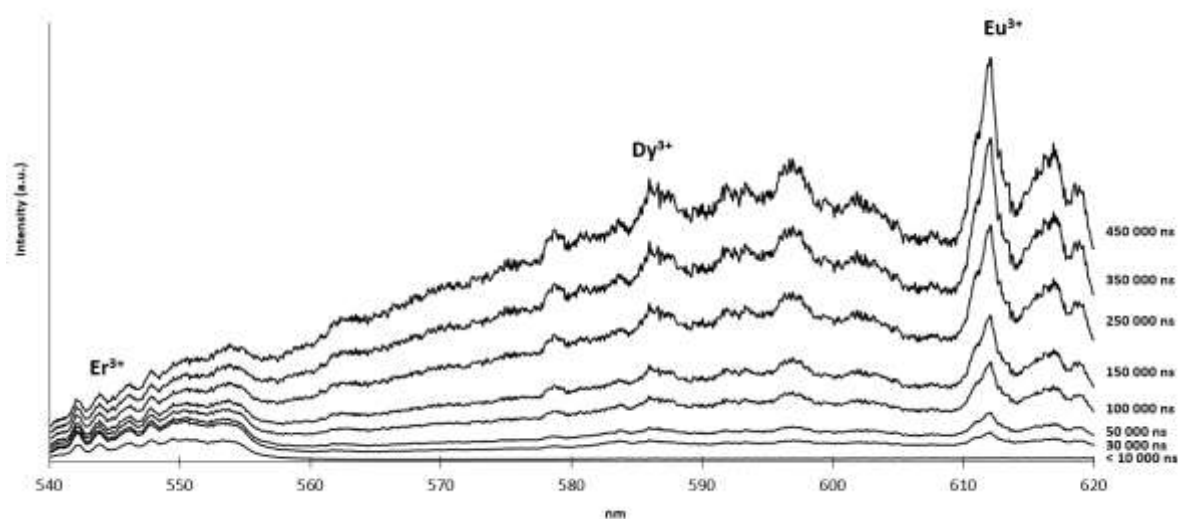


Fig.3: Luminescence spectra from a merrillite grain which gathered only the luminescence signal with an increasing gate width, from 10 000 to 450 000 ns at a constant delay (opening the gate just after the laser pulse).

Scanning Electron Microscopy

Scanning Electron Microscopy (SEM) investigations were performed on a Zeiss Ultra 55 field emission gun SEM (IMPMC, MNHN, Paris). The images were taken with the angle selective backscattered detector in the following conditions depending on the sample: 15 or 20 kV accelerating voltage, 7.5 to 8.3 mm working distance with the angle selective backscattered detector aperture of 25 to 120 μm , and high current. Energy-dispersive spectroscopy analyses and chemical maps were also acquired in those conditions. SEM was mainly used for a first-order characterization of mineral assemblages, as well as the dimensions of the microstructures.

5/ Results and discussion

5.1/ Raman investigations of the main silicate phases

5.1.1/ plagioclase Feldspar

Feldspars are nearly ubiquitous in Martian meteorites, and are useful to track geochemical and crystallization processes for most igneous rocks (Papike et al., 2009). The Martian surface, generally

considered to be dominated by basalts, is supposedly rich in plagioclase which was detected at many places using the Thermal Surveyor Spectrometer (TES) on board the Mars Global Surveyor mission (Christensen et al., 2001). Feldspars are an important mineral phase of the regolith breccia as they are present as crystal clasts, in all lithic clasts and in most impact-related spherules, and also as a major phase in the matrix (Hewins et al., 2017; McCubbin et al., 2016; Wittmann et al., 2015). Several geochemical investigations using electron microprobe (EMP) analysis report a feldspar composition ranging from K-rich feldspar [$\sim\text{An}_2 \text{Ab}_{14} \text{Or}_{84}$], usually found in differentiated clasts with monzonitic composition, to Na-rich [$\sim\text{An}_{25} \text{Ab}_{70} \text{Or}_5$] and Ca-rich [$\sim\text{An}_{42} \text{Ab}_{56} \text{Or}_2$] feldspar plagioclase, found in noritic and micro-basaltic clasts (Hewins et al., 2017).

Feldspars may be easily identified using Raman spectroscopy by a characteristic doublet of peaks with position varying between 470 cm^{-1} and 515 cm^{-1} depending on the mineral composition (Bersani et al., 2018; Freeman et al., 2008; Mernagh, 1991). The most intense peak is located around 510 cm^{-1} , accompanied by a less intense shoulder at $\sim 470 \text{ cm}^{-1}$. These peaks are labelled ν_a and ν_b successively according to the nomenclature used by Bersani et al. (2018). Weaker characteristic Raman bands can be found around 578 cm^{-1} (ν_c) and 290 cm^{-1} (ν_d). These four peaks are all related to various rotational and bending modes inside the tetrahedral framework. A suite of additional Raman modes can be detected below 450 cm^{-1} (i.e., around 450, 405, 354, 204, 176, 157 and 110 cm^{-1}) related to rotation-translation and external lattice modes (Freeman et al., 2008; Mernagh, 1991). Depending on crystal orientation, slight variations in the number of bands and their relative intensities may be observed.

CW Raman spectra were recorded for 16 points at exactly the same position previously analysed by EMP (Hewins et al., 2017). Some examples of representative CW Raman spectra and relevant SEM images are shown in fig. 4. Damage induced by previous LA-ICP analyses can be observed on some SEM images (Fig.4 a), but the spots for Raman analysis have been systematically placed far from these spots in order to avoid any structural damages due to previous analyses.

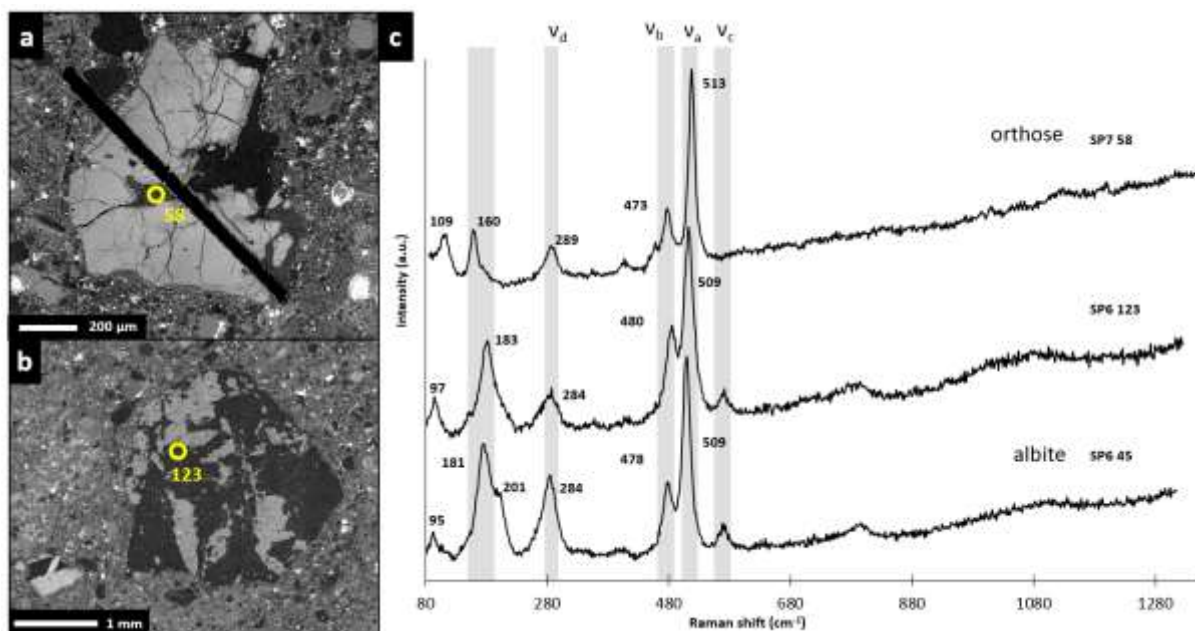


Fig. 4: Example of BSE images of various feldspars targeted with microprobe (EMP) and Raman spectroscopy (a, b), with associated CW Raman spectra (c). Note on the SEM image the trace of a previous footprint from an ICP ablation. The spectra are related to K and Na-rich feldspar; the position of their main Raman peaks is indicated.

All Raman spectra obtained on feldspars have the same general shape with some subtle variations. In detail, subtle changes in the Raman shifts of the main peaks can be observed between Na-rich (albite) and K-rich targets (orthose). K-feldspar spectra, like SP7 58 [$An_3 Ab_{10} Or_{87}$] (Fig.4 c), display major peaks at $\sim 513 \text{ cm}^{-1}$ and 474 cm^{-1} , whereas Na-rich feldspar main peaks are located at 509 cm^{-1} and 478 cm^{-1} . Furthermore, some differences are observed for the other peaks below 470 cm^{-1} . SP7 58 has 3 other peaks at $\sim 109, 160$ and 289 cm^{-1} while An-rich spots display different peak positions. SP6 123 [$An_{46} Ab_{52} Or_2$] actually displays peaks at 97, 183 and 284 cm^{-1} , whereas SP6 45 [$An_{27} Ab_{69} Or_4$] displays peaks at 95, 181, 201 and 284 cm^{-1} .

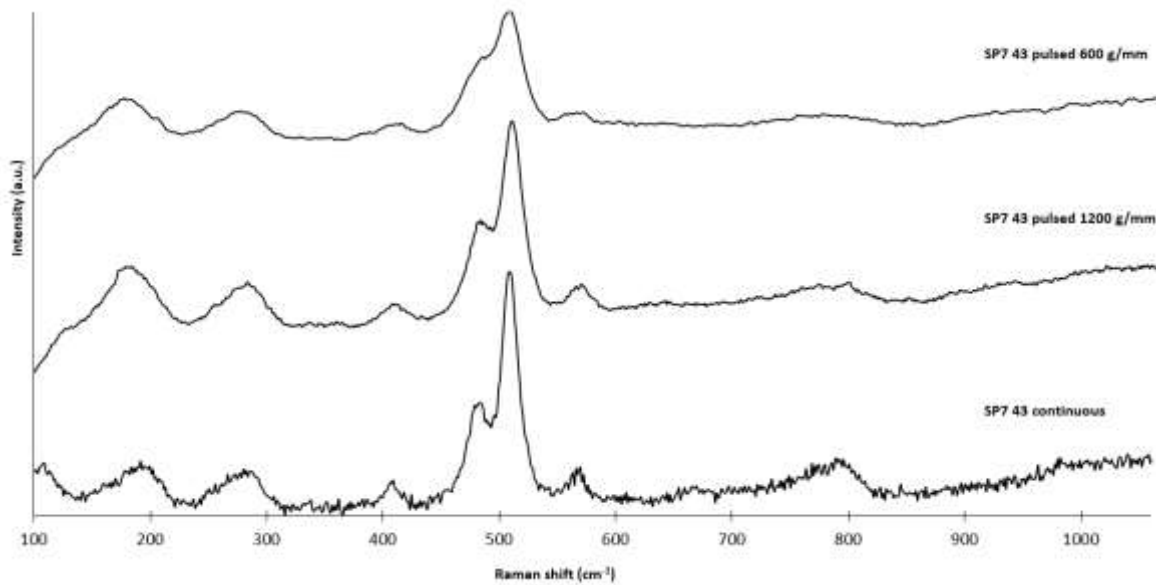


Fig. 5: CW and TR Raman spectra on the same feldspar (SP7 43). For the time-resolved spectra, two different spectral resolutions are used: 600 and 1200 g/mm gratings.

Furthermore, fig. 5 shows that CW Raman spectra and time-resolved spectroscopy with a short ICCD gate (Raman only, luminescence rejected) on the same target are very similar, even if in the TR spectra the peaks in the doublet are less visible due to the lower spectral resolution. This means that there is no detectable luminescence contribution to the spectra for these feldspars.

As a comparison with terrestrial samples, Freeman et al. (2008) described the Raman spectra of feldspar end-members and the influence of composition. They showed that the spectrum of K-feldspar $[\text{An}_1 \text{Ab}_{20} \text{Or}_{79}]$ exhibits main peaks at 513 and 475 cm^{-1} , very similar to the 513 and 473 cm^{-1} obtained in SP7 58 $[\text{An}_3 \text{Ab}_{10} \text{Or}_{87}]$. Similarly, their Na-rich feldspar $[\text{An}_{5.9} \text{Ab}_{93.8} \text{Or}_{0.3}]$ exhibits main peaks at 508 and 479 cm^{-1} , consistent with the peaks at 509 and 478 cm^{-1} from SP6 45 $[\text{An}_{27} \text{Ab}_{69} \text{Or}_4]$. The other points analyzed in the breccia have peaks with positions in the range of their compositional terrestrial analogs (Befus et al., 2018; Bersani et al., 2018; Freeman et al., 2008). However, small position shifts can be observed as our samples are not pure end-members. Considering other Martian data, similar plagioclase spectra are observed in several samples belonging to the SNC groups (such as Nakhla, Chassigny, Governador Valadarez, Lafayette and Yamato 000593), with peaks at 510-515 cm^{-1} and 477-480 cm^{-1} (Fritz et al., 2005). In some cases, all feldspar plagioclase can be partially or entirely transformed under high shock compression. For instance, maskelynite, has been observed in Martian meteorites and is helpful in tracing the shock history. Partial transformation in some meteorites results in peak broadening and upshifting, while maskelynite exhibits a very broad hump at higher wavenumbers in which the doublet may be hardly separated (Wang et al., 1999; Fritz et al.,

2005). Such features have not been detected in the breccia, in which there are no indications of shock except for melting.

5.1.2/ Pyroxenes

Pyroxene is a major mineral in Martian rocks, as it is widely detected *in situ* on its surface (Liu et al., 2022; Wiens et al., 2022) as well as from orbit (Mustard et al., 2005). Pyroxene is also common in SNC meteorites, and bears much information on Martian magmatic processes. It is a dominant mineral in the breccia, present as massive single-crystal shards, or associated with feldspar in various clasts. It is also a major component of the microcrystalline matrix. EMP analysis by Hewins et al. (2017) show that the composition is present as three phases: augite [$\sim\text{En}_{35}\text{Fs}_{25}\text{Wo}_{40}$], pigeonite [$\sim\text{En}_{52}\text{Fs}_{42}\text{Wo}_6$], and orthopyroxene [$\sim\text{En}_{68}\text{Fs}_{29}\text{Wo}_3$].

The Raman spectrum of pyroxenes has been described by Huang et al. (2000) and (Wang et al., 2001). This spectrum includes internal and external (lattice vibration) modes. We use the mode assignments given by Huang et al. (2000). The main peaks are located at about 1000 cm^{-1} (ν_{16} and ν_{17}) and 670 cm^{-1} (ν_{11} and ν_{12}). In pigeonite, the main peaks at $\sim 1000\text{ cm}^{-1}$ (ν_{16}) and $\sim 665\text{ cm}^{-1}$ (ν_{12}) have an asymmetric shape; it is caused by the presence of a shoulder next to ν_{16} towards high wavenumbers at $\sim 1020\text{ cm}^{-1}$ (ν_{17}), and towards lower wavenumbers next to ν_{12} at $\sim 655\text{ cm}^{-1}$ (ν_{11}). In some cases, the shoulder peak can be clearly distinguished from the main peak. A shoulder peak is not observed in augite. The first peak at $990\text{--}1010\text{ cm}^{-1}$ is assigned to the symmetric stretching mode of the vibration between the non-binding O and Si in the silicate tetrahedra. The second peak at $\sim 650\text{--}670\text{ cm}^{-1}$ range is assigned to the symmetric stretching vibration of the Si–O–Si bond in the silicate single chains. Several other peaks can be detected in the $300\text{--}400\text{ cm}^{-1}$ range which are due to lattice vibrations, in particular at $\sim 322\text{ cm}^{-1}$ (ν_3) for the Fe–O, $\sim 354\text{ cm}^{-1}$ (ν'_3) for the Ca–O and $\sim 390\text{ cm}^{-1}$ (ν_4) for the Mg–O interactions.

Representative CW Raman spectra performed at the same spot position as #25 EMP analysis from Hewins et al. (2017) [Supp table] are shown in fig.6 (c), with context images by SEM of corresponding targets in fig.6 (a,b). Some systematic changes occur between pigeonite and augite Raman spectra. Raman spectra of augite, like SP7 46 in Fig.6 (c), are characterized by two intense and narrow peaks around 664 cm^{-1} (ν_{12}) and 1011 cm^{-1} (ν_{16}), and additional weaker peaks at 323 , 358 and 389 cm^{-1} . Spectra of grains with pigeonite composition, like SP6 38 in fig.6 (c), display the same prominent stretching bands ν_{11} and ν_{16} at 672 cm^{-1} and 999 cm^{-1} . However, additional peaks at around 650 cm^{-1} (ν_{11}) and 1040 cm^{-1} (ν_{17}) are observed. Lattice vibrations are observed in both augite and pigeonite spectra with slightly varying positions reflecting different compositions. Augite generally exhibits the three peaks for lattice vibrations (ν_3 , ν'_3 and ν_4) while pigeonite only shows two peaks (ν_3 and ν_4) as the ν'_3 peak (Ca–O interactions) is absent in the Ca-poor pigeonite spectra.

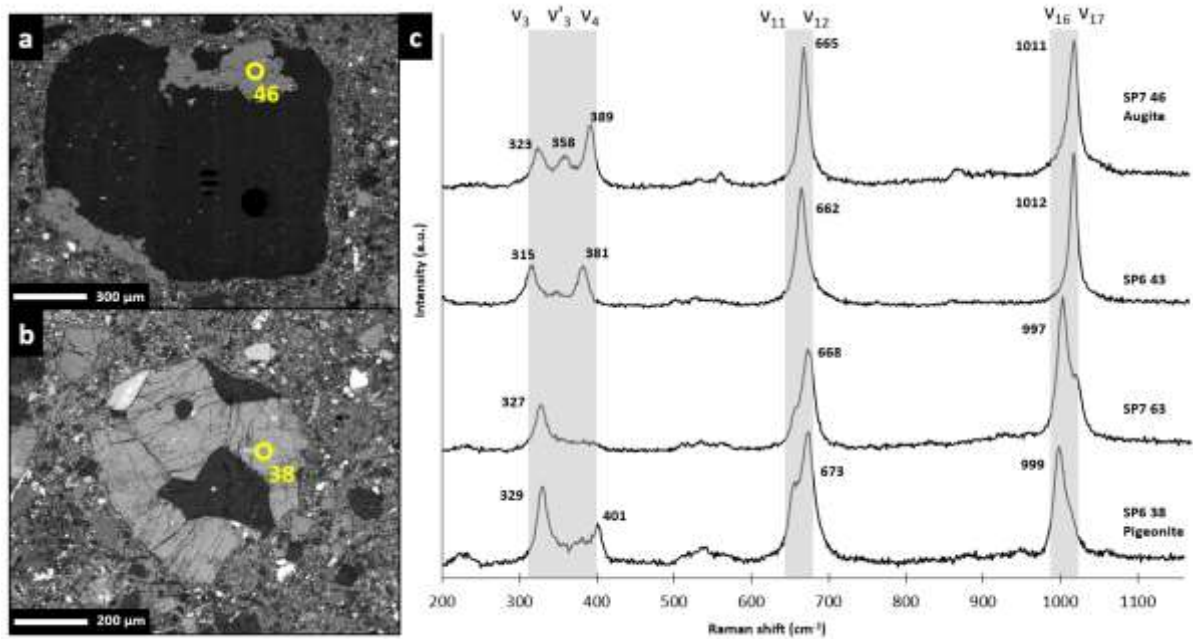


Fig.6: Examples of BSE images from pyroxene targeted with microprobe (EMP) and Raman spectroscopy (a, b), with associated continuous Raman spectra. These spectra are related to pigeonite and augite and the main peak's position is given.

Small shifts of peak position for v_{16} and v_{11} may be observed because of various cation contents in structural octahedral sites. Supplementary Figure *** shows that the peak position of peak v_{16} is correlated with FeO content based on EMP analysis: the peak position downshifts with increasing iron content. Similar impact of the FeO content has been described and discussed by Huang et al. (2000). Several other evolution trends can be observed between Raman peak frequency and cation content such as the v_{12} peak position increasing with MgO and FeO content, but decreasing with CaO. For the v_{16} peak, apart from FeO correlation, peak position tends to increase with CaO content.

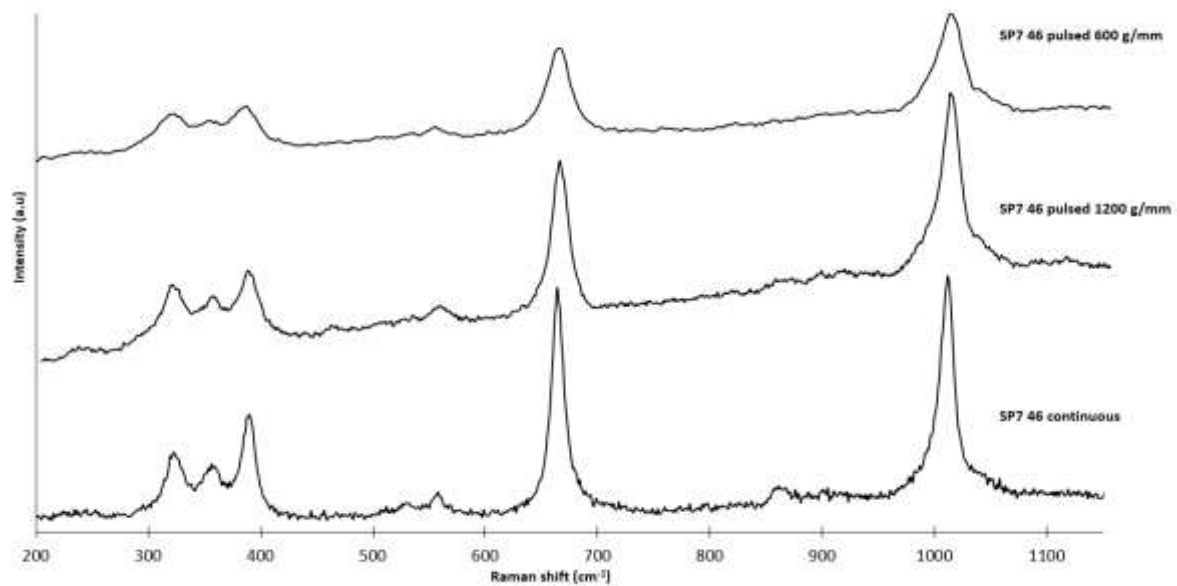


Fig.7: Continuous and Time-resolved Raman spectra on the same pyroxene (SP7 46). For the time-resolved technique, two different grids are used: 600 and 1200 g/mm gratings.

Furthermore, fig. 7 shows that Raman spectra obtained by CW and TR spectroscopy on the same analytical spot appear similar at first glance, as previously observed for the feldspar spectra. However, the peaks appear broadened with TR spectroscopy, with lower separation of the triplet at 300-400 cm^{-1} in augite due to the lower spectral resolution of this analytical setup. There is no significant luminescence signal observed in that spectral range for these pyroxenes.

There are several occurrences of exsolution-bearing pyroxene fragments in the breccia, with usually augite lamellae exsolved in bulk pigeonite (Wittman et al., 2015; Hewins et al., 2017). These lamellae are visible with SEM, and can be characterized by Raman hyperspectral mapping. An example of the Raman mapping of pyroxene exsolution is depicted in fig. 8 (a) where the different composition of the pyroxene is highlighted by the position of the ν_{16} peak in fig. 8 (b). Augite lamellae revealed by the Raman mapping closely match the patterns observed in the BSE image. Spectra extracted from the lamellae in fig. 8 (c) confirm their nature, augite rather than pigeonite, that is indicated by the darker color in BSE of the Fe-poor phase.

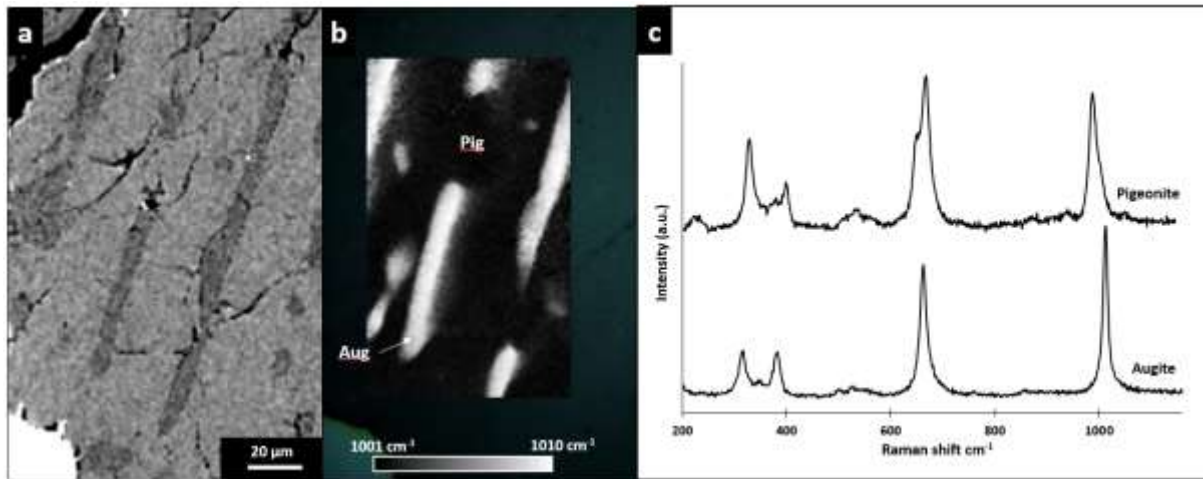


Fig.8: BSE (a) and Raman hyperspectral mapping (b) of -augite exsolution from pigeonite in NWA7533 SP7. The grey scale of the map is the position of the Raman peak ν_{16} around 1000 cm^{-1} , that varies with the composition. Hence, white patches reveal spectra with peaks around 1010 cm^{-1} , indicative of augite, and black patches correspond to low peak position, indicative of pigeonite. Spectra for augite and pigeonite (c) were extracted from the map to confirm the mineralogical nature.

Previous Raman investigations on different Martian SNC meteorites led to similar conclusions on Raman peak characteristics for augite and pigeonite (Mikouchi and Miyamoto, 2000; Rull et al., 2004; Wang et al., 1999, 2001, 2004a). In our data, peak position shifts of the most intense peaks can be observed down to a few cm^{-1} , explained by the variation of the structural cations, as described in depth by Huang et al. (2000) and Wang et al. (1997). Finally, Raman investigation of various pyroxenes in the breccia confirmed the absence of any shock-induced transformation of pyroxene, in agreement with the literature. Modifications by high-pressure processes should be visible in Raman spectra through significant peak broadening or the occurrence of amorphous glass (Zhang et al., 2018; Imae et al., 2010) which is not observed in our spectra. However, Leroux et al. (2016) observed some local shock microstructures inside pyroxenes at the nanoscale with TEM microscopy, which may be too small and/or scarce to be detected at the Raman scale of observation.

5.1.3/ Olivine

Olivine (and its polymorphs) is the major mineral of Earth's mantle and has been widely described in other planetary settings, from asteroids to other planetary bodies (Ody et al., 2013). On Mars, remote sensing (Hoefen et al., 2003; Mustard et al., 2005) and *in situ* investigations by rovers (Liu et al., 2022; Wiens et al., 2022) confirmed the presence of olivine. Thus, it is not surprising to find that most SNC Martian meteorites except basaltic shergottites contain olivine in various amounts, (Udry et al., 2020). Shergottites and chassignites tend to have more Mg-rich (forsterite end-member), while olivine in nakhlites are more Fe rich (Udry et al., 2020). On the other hand, there are a few examples of Martian meteorite lithologies where olivine is absent. Apart from ALH84001, a pyroxene cumulate, NWA 7533 and paired breccia samples are almost completely free of olivine, with only a few reports of olivine dendrites inside some melted impact spherules (Hewins et al., 2017; Udry et al., 2014).

These rare olivine dendrites are really thin ($\sim 10 \mu\text{m}$) and elongated, suggesting rapid cooling processes. However, not every vitrophyric spherule found in the breccia contains such olivine crystals.

In olivine, vibrational modes of the SiO_4 tetrahedron will cause the distinct bands in the Raman spectra. The most characteristic are a doublet of peaks between 815 cm^{-1} and 860 cm^{-1} triggered by symmetric (ν_1) and asymmetric (ν_3) stretching modes (William, 1995). Symmetric (ν_2) and asymmetric (ν_4) bending of the SiO_4 tetrahedra will result in peaks between 400 cm^{-1} and 700 cm^{-1} , with peaks below 400 cm^{-1} usually attributed to transitional or rotational movements in the crystalline lattice. Slight differences occur relative to the variation of Mg^{2+} or/and Fe^{2+} content. For a forsterite composition, the ν_1 and ν_3 peaks are clearly distinct, while they are closer in wavenumber and less distinct for fayalite spectra. Kuebler et al. (2006a) calibrated an equation to determine the %Fo composition of olivine as a function of the position of the main Raman peaks.

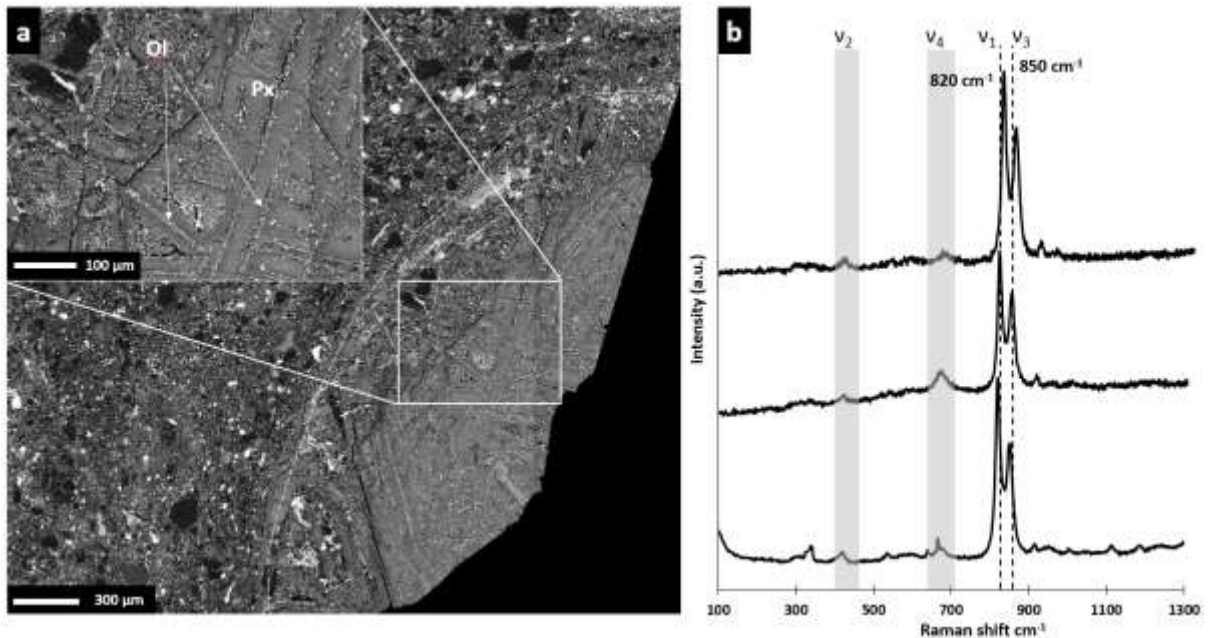


Fig. 9: BSE images of a melted spherule outlined by a dotted line in NWA7533 SP2, with a close-up of elongated olivine (Ol) dendrites surrounded by microgranular pyroxenes (Px) show in A. CW spectra from this olivine are shown in B with the main Raman peaks outlined. The distinct doublet is easily recognizable, with values being rather constant, with $819\text{-}820 \text{ cm}^{-1}$ for ν_1 and $849\text{-}850 \text{ cm}^{-1}$ for ν_3 .

Several olivine dendrites were analyzed in a single spherule, shown in detail in fig. 9 A. The results appear to be highly homogeneous, with all analyzed olivine dendrites displaying distinct ν_1 and ν_3 doublet peaks at $819\text{-}820 \text{ cm}^{-1}$ and $849\text{-}850 \text{ cm}^{-1}$. These values are in the range of Mg-rich olivine compared to investigations from Weber et al. (2014) and Kuebler et al. (2006a) from different terrestrial and planetary environments. Investigations of Martian meteorites give comparable results, with exact similar peak position (820 and 850 cm^{-1}) in a shergottite with Mg-rich forsterite (Wang et al., 2004a). In addition, using the equation from Kuebler et al. (2006a) with the ν_3 peak position, we were able to determine a Fo $_{73-65}$ composition. Other studies in the breccia obtained similar and

consistent results using EMP analysis: Fo₇₄₋₆₅ (Hewins et al., 2017 in NWA7533), Fo₆₅₋₅₃ (Udry et al., 2014 in NWA7034). Finally, our Fo composition of olivine in the breccia is similar to those found *in situ* with rovers in Jezero crater (Liu et al., 2022; Wiens et al., 2022) and in Gusev crater (McSween et al., 2008), but it is clearly not in the same petrologic setting.

5.2/ Raman and luminescence of secondary minerals

5.2.1/ Phosphates: apatite and merrillite

Phosphates are known to be an important component of Martian rocks: they are detected from orbit (Christensen et al., 2002), and *in situ* by the ChemCam LIBS instrument aboard the Curiosity Rover (Cousin et al., 2017), and by the PIXL instrument aboard Perseverance (Liu et al., 2022). Phosphates are also observed in many different Martian SNC meteorites (Borg, 2005; Wang et al., 1999, 2004a) 2004a), also reported in the breccia (Bellucci et al., 2015; Hewins et al., 2017; Hu et al., 2019; McCubbin et al., 2016; Smith et al., 2020) and in the ALH 84001 pyroxenite (Cooney et al., 1999). As an efficient reservoir for trace elements and water, phosphates are key targets for dating or studying magmatic and alteration processes. The dominant phosphate in Martian meteorites is apatite Ca₅(PO₄)₃(OH, Cl, F), mostly Cl-rich chlorapatite and some F-rich fluorapatite. Apatite is found as individual grains or grains in clasts, but also as a minor component of the microcrystalline matrix. Apatite is often locally associated with other minerals in many clasts from differentiated monzonitic and noritic clasts to microbasaltic fragments, displaying a large diversity of microtexture. In addition, merrillite (ideally Ca₁₈Na₂Mg₂(PO₄)₁₄) is rarely found in the breccia, and is systematically microtexturally associated with apatite.

Phosphates such as apatite and merrillite have characteristic yet distinct Raman spectra. Their Raman spectra have been described in terrestrial and extraterrestrial samples (Fau et al., 2022; Jia et al., 2020; Jolliff et al., 2006, 1996; Litasov and Podgornykh, 2017; O'Shea et al., 1974). The symmetric stretching vibration mode of PO₄³⁻ provide the most intense Raman peak between 950-990 cm⁻¹, labelled as ν_1 . Apatite has a single ν_1 band at 964 cm⁻¹, and merrillite has a doublet of peaks around 955 and 975 cm⁻¹. Other less intense peaks can be observed in the apatite spectrum caused by internal modes in PO₄³⁻. The doubly generated ν_2 bending mode is located at ~430 cm⁻¹, the triply generated antisymmetric ν_3 stretching band is at ~1060 cm⁻¹, and finally the triply generated bending mode ν_4 can be detected at ~580 cm⁻¹. OH⁻, when present, contributes with a large band at ~3570 cm⁻¹.

The presence of other elements at trace level like Mn²⁺ or trivalent Rare Earth Elements (REE) inside the crystal lattice can produce luminescence bands in the Raman spectra, induced by laser excitation (Fau et al., 2022). Examples of such bands are: Er³⁺ (540-550 nm), Dy³⁺ (590 nm), Eu³⁺

(570 – 580 nm) and Sm^{3+} (560-570 nm and 600 nm). Mn^{2+} is characterized by a very broad emission centered at 595 nm generating a huge background in Raman spectra. This luminescence signal is often observed in natural phosphates and has been well described by Gaft et al. (2015) and Fau et al. (2022). Here, we focus first on the Raman and luminescence spectra from a specific grain including both apatite and merrillite, and then we expand the discussion to diverse apatite grains. In all the phosphate grains investigated, we never detected an OH band suggesting that the water content of these phosphates is negligible.

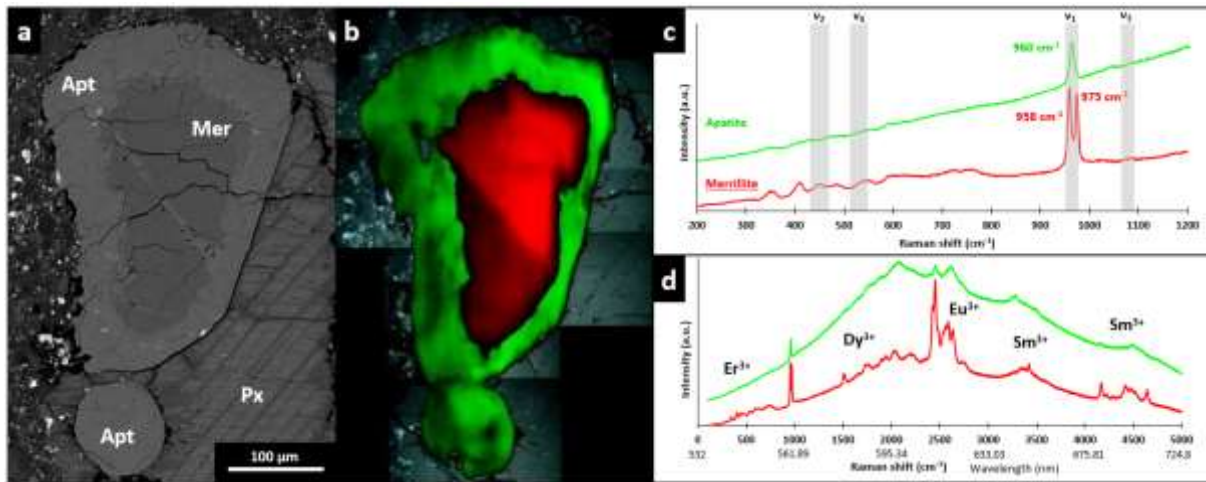


Fig. 10: BSE (a) and Raman map (b) of a grain apatite (green) rimming merrillite (red), with representative Raman spectra (c) with highlighted Raman bands indexation. The luminescence signal is illustrated on merrillite and apatite spectra, from 0 to 5000 cm^{-1} (d), with luminescence band associated with the presence of Er^{3+} , Dy^{3+} , Eu^{3+} and Sm^{3+} .

Figure 10a shows a large phosphate grain including two different phases based on the contrast in BSE image. CW Raman, hyperspectral imaging (Fig. 10b) and point spectroscopy (Fig. 10c) shows that the core of the grain is composed by merrillite while the external part is composed by apatite. Merrillite shows the characteristic ν_1 doublet with peaks at 958 and 975 cm^{-1} ; the position being constant all over the merrillite grain. The relative intensities of the two peaks in the doublet vary between two parts of the grain but is relatively constant in each part. This could reflect the presence of two domains in the grain with slightly different crystallographic orientation. In the apatite rim, peak position, FWHM and intensity of the ν_1 peak is constant throughout the whole grain. Figure 10d depicts representative CW spectra including luminescence and Raman for apatite and merrillite. The two spectra bear strong similarities with clear luminescence bands reflecting the presence of REE³⁺ in the crystal lattice. A broad background band centred at $\sim 595 \text{ nm}$ is possibly due to the luminescence of Mn^{2+} . This is consistent with the detection of trace amounts of Mn in the breccia phosphates by Hu et al. (2019) (0.07 to 0.17 wt% of MnO). This suggests that the two mineral phases hold a similar diversity and content of REE. Both BSE and Raman images can be interpreted as the replacement of apatite over pre-existing merrillite, as apatite is external compared to merrillite in the phosphate grain,

and the transition between apatite and merrillite is sharp yet the boundary is irregular in the grain. Such replacement scenario fits well with the similar REE patterns in apatite and merrillite.

A textural survey of apatite grains in the breccia highlights the diversity of morphologies of apatite grains and petrological settings where apatite is found. For instance, massive elongated grains can be found in several clasts of monzonitic and noritic composition, visible in fig.12 a, c. Thin needles of apatite several hundreds of μm in length and $\sim 5 \mu\text{m}$ wide are also found in different clasts associated with feldspar (fig.12 b,d). Raman spectra exhibit constant ν_1 peak position and FWHM among the diverse morphologies (Fig.12 e): position range between 960 and 961 cm^{-1} . Such a peak position is consistent with the dominant presence of chlorapatite in agreement with literature (Hewins et al., 2017; Hu et al., 2019; McCubbin et al., 2016). Only one exception was found with ν_1 around 963 cm^{-1} , likely corresponding to a fluorapatite (Černok et al., 2019). All apatite exhibits a broad background centered at $\sim 595 \text{ nm}$ likely due to the presence of trace amounts of Mn^{2+} in the crystals. Some apatite displays weak REE luminescence peaks superimposed on the Mn^{2+} signal.

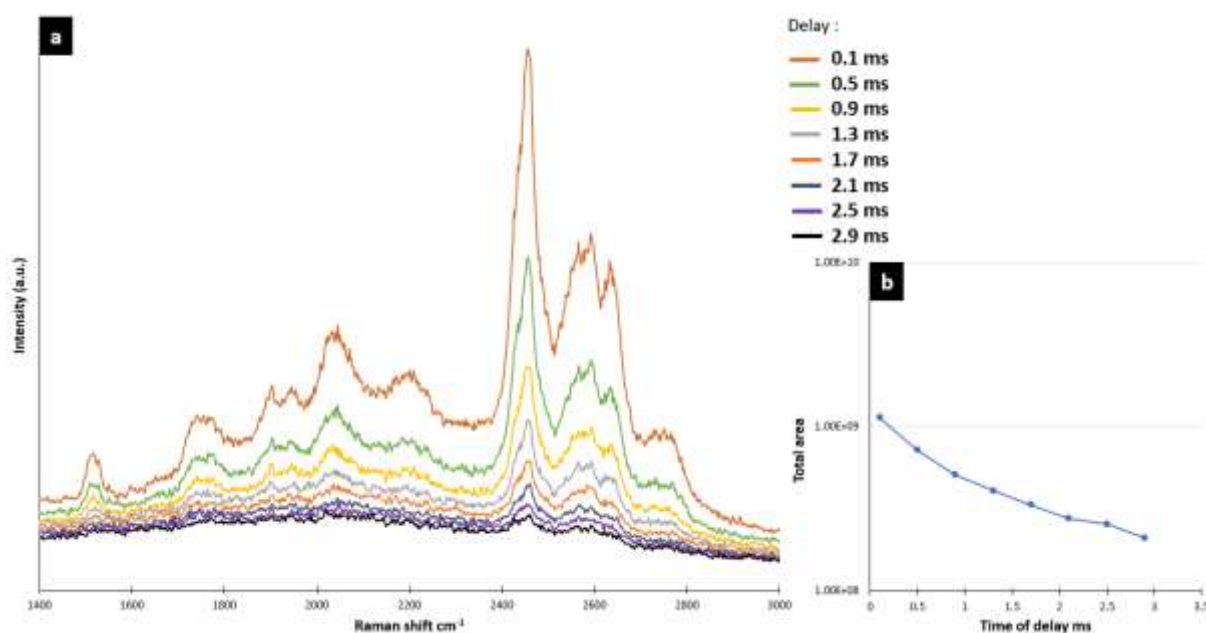


Fig.11: Time-sweep experiment to determine the decay lifetime of Eu^{3+} in merrillite. Cumulated spectra on the Eu^{3+} pattern of a merrillite, each with a $400\,000 \text{ ns}$ gate width and a $40\,000 \text{ ns}$ gate delay increment (a). The total area under the peaks in each spectrum is then plotted against the time, showing a gradual decrease (b).

A luminescence signal is detected in some Raman spectra. Figure 10d illustrates the presence of REE in an apatite crystal. However, such bands are not observed in some spectra, suggesting heterogeneities in REE enrichment among the apatite grains. Using time-resolved spectroscopy on apatite and merrillite, it is possible to obtain Raman spectra without a luminescence contribution, but also luminescence spectra without a Raman contribution, so as to analyse the luminescence signal.

Such analyses confirm the presence of REE³⁺ such as Er³⁺, Dy³⁺, Eu³⁺ and Sm³⁺ (see fig. 2). It is also possible to measure the time decay of luminescence by isolating a peak specific of a given REE. The luminescence pattern of Eu³⁺ in a merrillite grain was isolated and several spectra with a gradual increase of delay for the ICCD gate opening were analysed and are shown in fig.2. The total intensities of the luminescence peaks can then be represented against the gate delay (fig.11b). The lifetime is then calculated as the slope of the line going through the experimental points, giving a value of 0.56 ms. (Fau et al., 2022) revealed a linear correlation between lifetime and Eu concentration inside synthetic apatite. Here we obtain a lower value compared to the lifetime in apatite. That may be due to the different decay lifetime of Eu³⁺ in the merrillite structure but also to energy transfers between the various luminescence activators present in the crystal lattice (Fau et al., 2019).

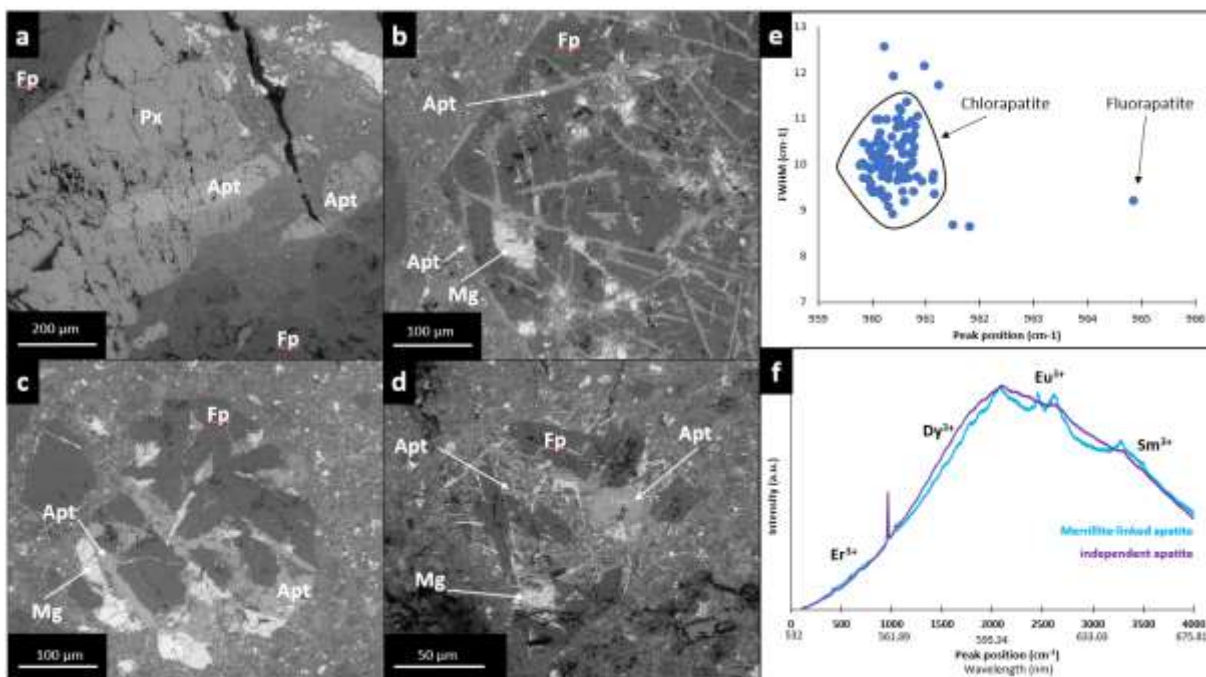


Fig.12: BSE images of different apatite morphologies in clasts found around the breccia (a, b, c, d), associated with the different mineral phases: Px = Pyroxenes, Fp = feldspar, Apt = apatite, Mg = magnetite. The Raman survey of these different apatite crystals is summarized in e, with the position vs FWHM of the ν_1 Raman peak, where most of the data are homogenous. However, the luminescence signal survey (f) gives different results, with luminescence patterns different between the apatite around the merrillite and the other apatite grains.

Our Raman results are in line with Raman investigations on different martian SNCs, with ν_1 peak position values clustering around 960 cm^{-1} and no hydration detected suggesting the dominance of chlorapatite. For merrillite, our spectra are highly similar to those obtained by (Wang et al., 1999, 2004a) on shergottites with peak positions of 958 and 975 cm^{-1} for the merrillite doublet. Additionally, we did not detect any evidence for high pressure structural modification of phosphates, such as a broadening of the main ν_1 Raman peak or the presence of high-pressure phosphate phase like whitlockite. Our investigations reveal the likely presence of at least two generations of phosphates in

NWA7533. The first one crystallized initially as merrillite and was later transformed to apatite probably during a metasomatic event during which merrillite interacted with fluids. With our data we cannot specify how and when this metasomatic event happened. The other generation of apatite covers all other apatite grains which are not linked to the presence of merrillite based on textural identification of merrillite or inherited REE luminescence from prior merrillite. This group covers a wide diversity of textures and could actually be subdivided in several groups corresponding to various crystallization processes (magma source, cooling rate...).

5.2.2/ Zircon

Zircon (ZrSiO_4) is a highly resilient accessory mineral found inside magmatic, metamorphic and sedimentary rocks, crucial for geochronological purposes. It is the oldest mineral found on Earth with ages up to 4.4 Gyr for the Jack Hills zircon grains (Peck et al., 2001; Wilde et al., 2001). Upon the discovery of zircon in NWA 7533 and paired breccia samples, U-Pb ages revealed crystallization processes as old as 4.4 Gy, with a major heating event around 1.7 Gy (Hu et al., 2019; Humayun et al., 2013). These zircons are found throughout the different components of the breccia, from the matrix to the various clasts, and can be very heterogeneous in size, shape and structural state.

The Raman signature of zircon has been described in detail by Dawson et al. (1971), Syme et al. (1977) and Nasdala et al. (2001). We use the peak assignment from these studies. Vibration modes in the SiO_4 tetrahedron induces 4 main distinct peaks, with bending modes around 439 cm^{-1} (ν_2) and 350 cm^{-1} (ν_4) and stretching modes around 975 cm^{-1} (ν_1) and 1000 cm^{-1} (ν_3). Additional modes caused by lattice vibrations can be found around 200 cm^{-1} . The asymmetric stretching band ν_3 is generally the most intense and distinct peak in the zircon spectrum. Alteration due to radiation damage induced by high U content (Pellas, 1954) can be traced through variation of position, intensity and FWHM of this peak, as described by Nasdala et al. (2002, 2001). Low FWHM values and higher peak position indicate a high degree of crystallinity, while wider peaks with down-shifting position values reflect increasing degree of alteration. Luminescence bands, often caused by trivalent REE, like Sm^{3+} , Eu^{3+} , Dy^{3+} and Er^{3+} , can also be observed in certain zircons.

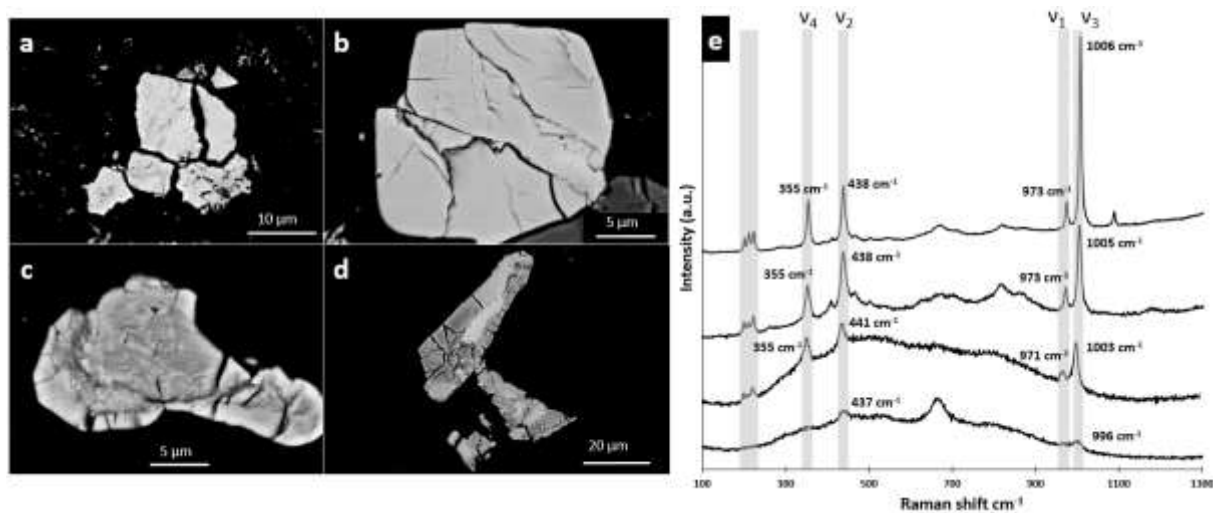


Fig. 13: BSE images from zircons in several polished section of NWA 7533 displaying either a homogeneous aspect (a & b) or heterogenous domains (c & d). Note that zircon a has a lot of small textural perturbations, while zircon b seems pristine over all of its surface. Various CW zircon Raman spectra (e) illustrate their structural diversity, with the spectra most indicative of crystalline form (top) associated with the clearest textural surface, gradually evolving towards damaged spectra (bottom), which are obtained from heterogeneous and amorphous domains.

Figure 13 depicts some representative microtextural habits of zircons in NWA7533: some zircons display a pristine smooth surface while others exhibit complex patterns with alternance of rough and smooth areas. This textural variability is coherent with the different Raman spectra obtained from these different zircons and domains. Fig.13 e shows the diversity of Raman spectra. The most pristine spectra are obtained on the smooth and homogenous surface domains: they have a ν_1 peak position at 1006 cm^{-1} and FWHM of 6 cm^{-1} indicative of high crystallinity. Other spectra obtained on domains with rough and heterogenous surfaces show increasing degrees of alteration, with the peak downshifting (down to 1000 cm^{-1} in position) and broadening, and an increasing broad background signal in the range of ~ 300 to $\sim 1000\text{ cm}^{-1}$. Furthermore, some zircons exhibit a luminescence signal due to the presence of REE³⁺. TR spectroscopy (fig. 14) is used to confirm the presence the luminescence nature of these peaks by excluding the Raman signal with time resolution (Fig. 14). The presence of Sm³⁺ could explain the presence of these two peaks between 2200 cm^{-1} (602.52 nm) and 2600 cm^{-1} (617.4 nm).

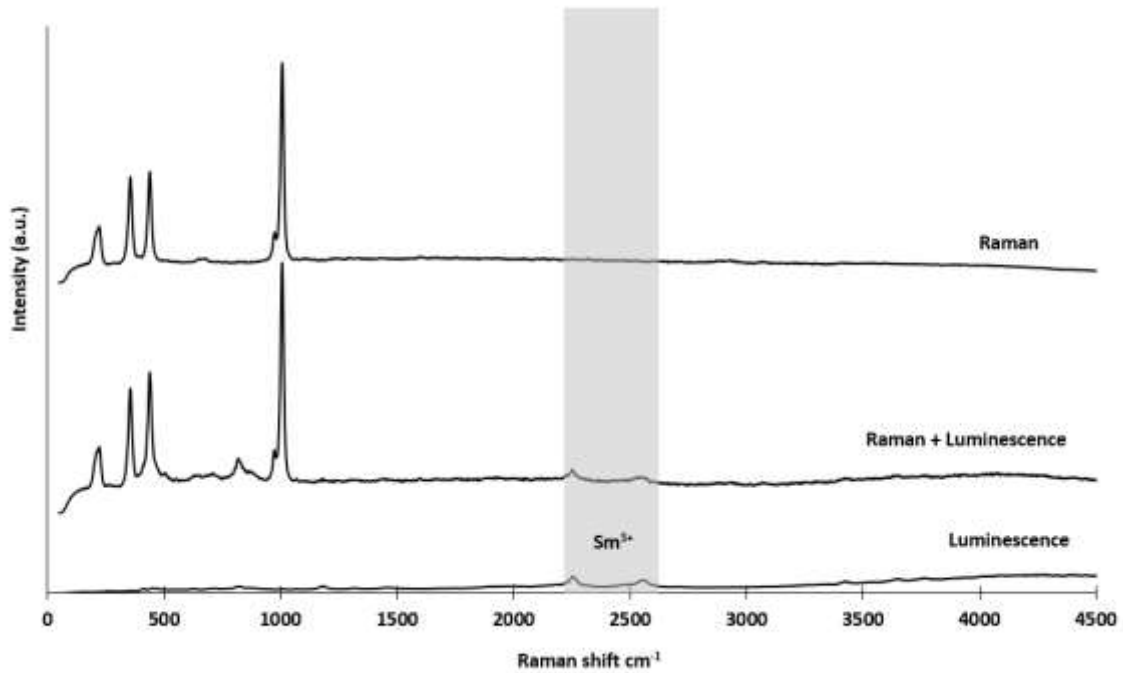


Fig. 14: Time resolved Raman spectra from a single well crystallized zircon grain. Only the Raman signal was gathered for the uppermost spectra, using a very short gate width. The spectrum in the middle is the standard Raman and luminescence signal, and the last spectra is obtained by collecting the luminescence spectra, with some faint peaks associated with a weak Sm^{3+} abundance.

Results from CR and TR Raman spectroscopy investigations on several zircons from the breccia revealed huge structural heterogeneities. Raman peak characteristics are comparable to terrestrial standards from Nasdala et al. (2001) showing distinct trends in position and FWHM values in relation with the amount of damage induced by metamictization processes. This observation agrees well with other in-depth studies of zircon in the martian breccia: Hu et al. (2019) and Roszjar et al. (2017) observed similar zircon spectra, either well crystalline or deeply damaged. Specifically, they confirmed the presence of highly heterogeneous zircon displaying both crystalline and amorphous domains in a single grain, similar to the BSE images in fig.13cd, which are not related to impact texture. Indeed, none of the zircon investigated seems to have undergone significant shock processes due to the lack of any shock-induced morphologies, like the rest of the minerals from the breccia. A rare exception of a shocked zircon was observed in the breccia by Cox et al. (2022).

5.2.3/ oxides

Opaque phases can provide information upon the conditions of formation and alteration of a sample. Such Fe-Cr-Ti rich phases can be associated with accessory minerals like zircon in most magmatic rocks. Several oxides have been reported in the Martian breccia, composing the bulk matrix or associated with other minerals inside several clasts. Almost 15 wt% of the breccia is magnetite,

bearing the majority of the strong magnetic signal of the sample (Gattacceca et al., 2014), accompanied by a suite of Fe-Cr-Ti oxides (Hewins et al., 2017; McCubbin et al., 2016; Santos et al., 2015). Here we report the Raman investigations on magnetite ($\text{Fe}^{2+}\text{Fe}^{3+}_2\text{O}_4$), ilmenite (FeTiO_3), hematite (Fe_2O_3) and rutile (TiO_2) found in several section of the breccia. Due to their association with pyrite, hematite spectra are discussed in the following section,

The Raman signatures of the most common oxides have been reviewed by (Frezzotti et al., 2012). In magnetite, only the sites occupied by Fe^{3+} and O^{2-} ions contribute to the Raman activity (Shebanova and Lazor, 2003), resulting in a characteristic strong peak at $\sim 668 \text{ cm}^{-1}$ accompanied by another band at $\sim 538 \text{ cm}^{-1}$. Two weaker bands are observed at $\sim 306 \text{ cm}^{-1}$ and $\sim 193 \text{ cm}^{-1}$. Ilmenite is characterized by a strong Raman peak at $\sim 685 \text{ cm}^{-1}$, associated with weaker bands at $\sim 373 \text{ cm}^{-1}$ and 232 cm^{-1} (Rull et al., 2007). Finally, Rutile is defined by two strong peaks at ~ 609 and $\sim 444 \text{ cm}^{-1}$, accompanied by weaker bands at $\sim 920 \text{ cm}^{-1}$, 696 cm^{-1} , 238 cm^{-1} and 139 cm^{-1} . CW spectra were acquired on various oxides encountered in our investigations as well as on several magnetite grains characterized with EMP by Hewins et al. (2017). SEM chemical mapping was used to confirm the presence of Fe, Ti or Cr in some of the newly investigated grains.

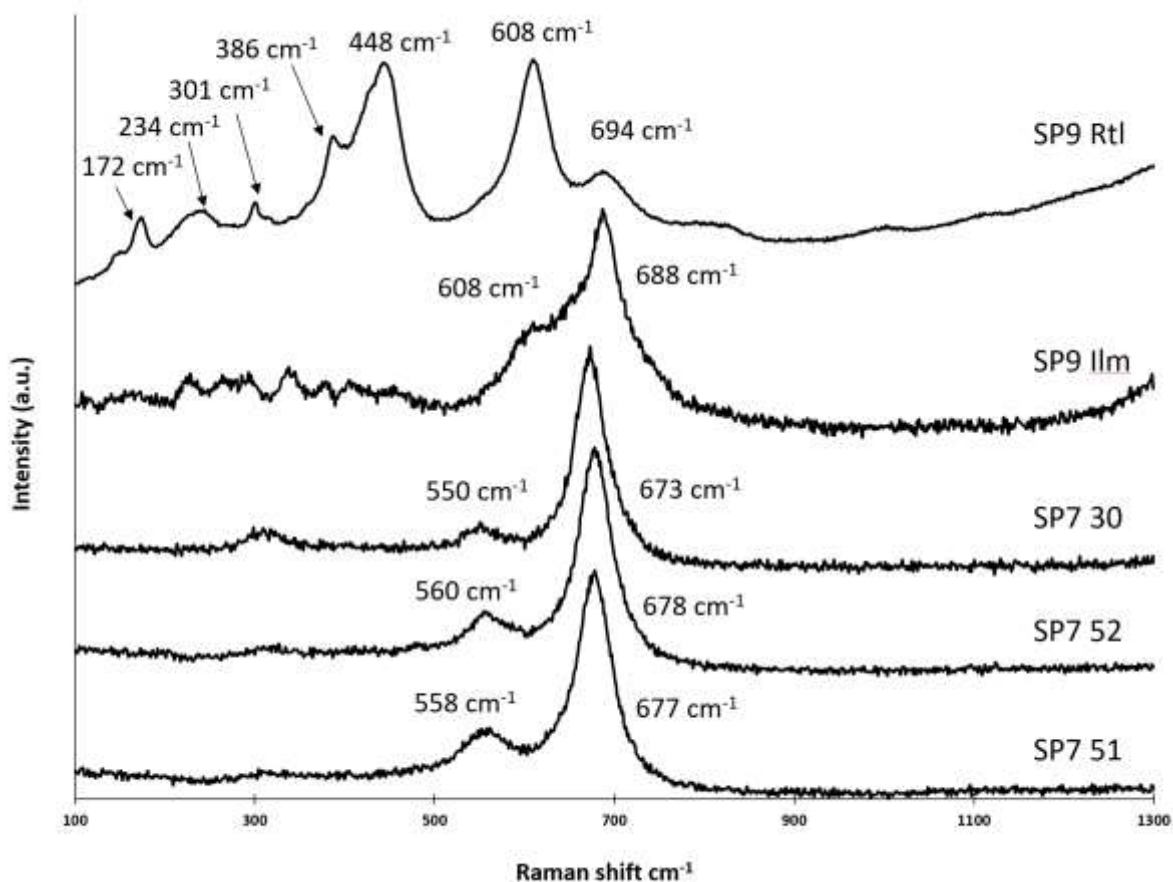


Fig. 15: CW Raman spectra illustrate the different Fe-Ti oxides encountered in the Breccia. SP7 30, 52 and 51 were previously analyzed with EMP, highlighting their magnetite composition. SP9 Ilm and SP9 Rtl spectra were obtained on an assemblage of Fe-Ti and Ti oxides, identified with chemical cartography using SEM.

Figure 15 depicts the diversity of oxide spectra encountered. At the bottom, three spectra (SP7 51, SP7 52 and SP7 30) exhibit strong bands at 673-678 cm^{-1} , accompanied by a weaker band at 550-560 cm^{-1} . EMP analysis by Hewins et al. (2017) show that two spots are Ti-magnetite: SP7 30 [$\sim\text{Spin}_5\text{Chrom}_1\text{Usp}_{23}\text{Mgt}_{68}$] and SP7 52 [$\sim\text{Spin}_0\text{Chrom}_0\text{Usp}_{13}\text{Mgt}_{85}$]. SP7 51 [$\sim\text{Spin}_6\text{Chrom}_{31}\text{Usp}_{51}\text{Mgt}_{12}$] is a Ti-Cr spinel, yet the position range of the main peaks remains coherent with the previous points. The SP9 Ilm comes from a Fe-Ti-rich oxide and exhibits a strong Raman band at 688 cm^{-1} , close to the peak of ilmenite. Hence, this oxide was labelled as an ilmenite. However, the systematic presence of a weaker 608 cm^{-1} Raman band in every observed Fe-Ti-rich oxide doesn't completely match the ilmenite spectrum. Such a peak could be explained by the presence of small amounts of rutile in the grain. The spectrum SP9 Rtl was obtained next to SP9 Ilm on a Ti-rich oxide. It displays intense peaks at 608 cm^{-1} and 448 cm^{-1} , with weaker bands at 694, 386, 301, 234 and 172 cm^{-1} . This description matches the spectra of rutile described by Frezzotti et al. (2012).

The magnetite spectra have a similar aspect to other (terrestrial) samples (Frezzotti et al., 2012; Shebanova and Lazor, 2003), but our position values are up-shifted from 5 to ~ 10 cm^{-1} from their values. Similarly, position values from magnetite in a shergottite in (Wang et al., 2004b) are lower than our results. This could be explained by a stronger Usp (ulvöspinel [Fe_2TiO_4]) contribution in the oxide composition from SP7, the spectrum of ulvöspinel being characterized by a ~ 680 cm^{-1} main Raman peak. Our results are consistent with other studies of the Raman spectra of the different oxides in the breccia (McCubbin et al., 2016).

5.2.4/ Pyrite and its associated alteration phases.

Pyrite (FeS_2) detection and characterization can help us understand the magmatic and alteration history of a rock. Sulfide minerals have been thoroughly studied on Mars, the sulfur cycle being one of the most important geochemical cycles on the planet (Franz et al., 2014). Global Mars survey suggest a surface abundance of 4.40 wt% SO_3 on the surface (Dyar et al., 2011). Comparatively, pyrite composes up to 1% of the Martian breccia by weight, as a component of the matrix and of certain clasts. It has been a key mineral to constrain late-stage alteration processes in the sample (McCubbin et al., 2016). It is inferred that the pyrite formed during the low temperature thermal event recorded at ~ 1.7 Ga. Afterwards, they underwent light shock deformation like planar fractures, which acted as preferential pathways for partial alteration of the pyrite mainly to iron oxyhydroxide during its stay in the Sahara Desert (Lorand et al., 2018, 2015).

The Raman spectrum of pyrite has been studied in detail by Mernagh and Trudu (1993). They assigned 3 main Raman active modes to isotropic pyrite crystals. The most intense peak is at ~ 387 cm^{-1}

¹, followed by peaks at $\sim 353\text{ cm}^{-1}$ and 446 cm^{-1} . An anisotropic form of pyrite displays shifted peaks with broadened aspect at $\sim 377\text{ cm}^{-1}$, $\sim 342\text{ cm}^{-1}$ and $\sim 428\text{ cm}^{-1}$. Hematite inside the breccia pyrite alteration phases is recognizable by several Raman peaks described by Kuebler et al. (2006b) and (Frezzotti et al., 2012): intense peaks are located at ~ 1313 , ~ 409 , ~ 290 and $\sim 223\text{ cm}^{-1}$, usually followed by minor peaks at 498 and 609 cm^{-1} . Several CW spectra were acquired on pyrite and surrounding alteration phases, recognizable under the microscope with reflected light and by BSE images. A Raman map was also extracted in order to trace possible compositional variation in the alteration phase.

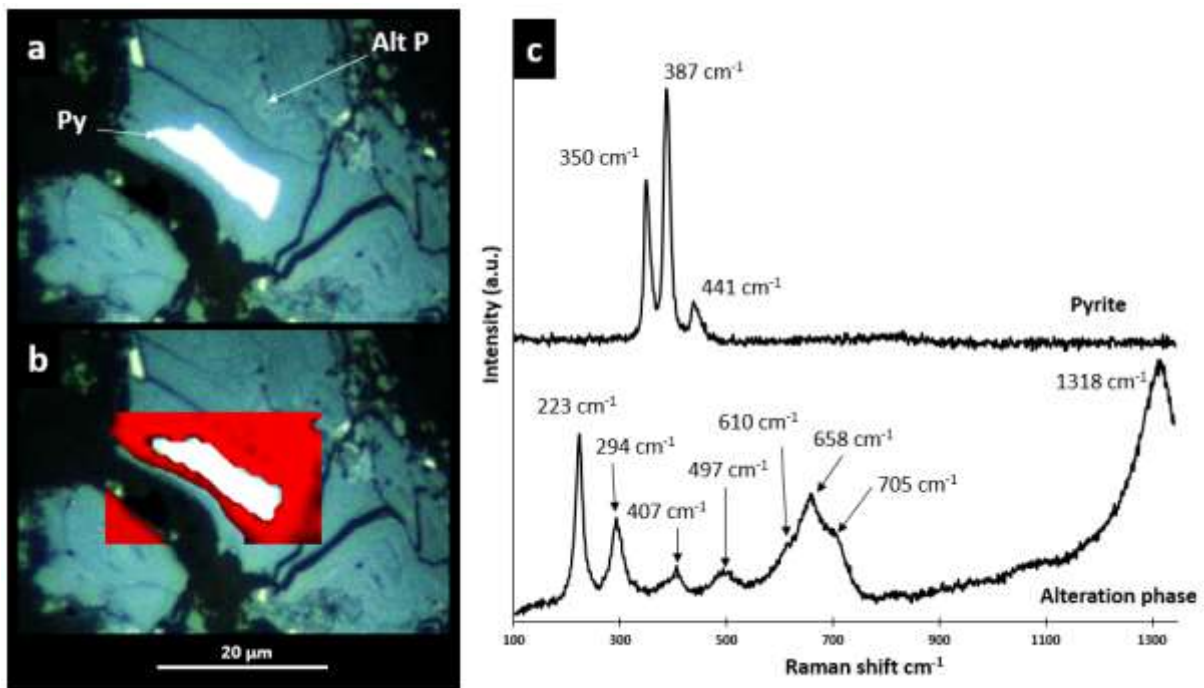


Fig. 16: Reflected light image (a) of a pyrite (Py) surrounded by its alteration phases (Alt P), paired with the Raman cartography (b) highlighting the presence of the altered pyrite in red. The representative CW Raman spectra of pyrite and its alteration phase are shown in c with their peak position.

Figure 16 (a) shows a reflected light image of a pyrite, in bright white, surrounded by its alteration phase, with a distinct greyish colour and a layered texture. The Raman map (fig.16 b) extracted around the pyrite grain show that the surrounding altered pyrite is homogenous, with consistent Raman spectra. Figure 16 (c) show detailed Raman spectra of a pyrite and its alteration phase. The pyrite Raman spectra display clear and intense peaks at 350 and 387 cm^{-1} with a lower peak at 441 cm^{-1} . These values are constant throughout the different grains investigated. The Raman spectra of the alteration phase is more complex with a multitude of peaks. Several peaks at 1318 , 610 , 498 , 409 , 290 and 223 cm^{-1} are very close to the values of the hematite Raman peaks described earlier, confirming its presence around the pyrite. Additional peaks at 658 and 705 cm^{-1} are not found in hematite spectra, and is likely due to the presence of another iron oxyhydroxide. Its nature has not been identified and remains unknown. Gattacceca et al. (2014) reported goethite in the breccia

transforming to hematite during heating experiments. We did not see spectral evidence of maghemite or goethite in the alteration material analysed.

The pyrite spectrum obtained in the breccia is very similar to the spectrum obtained on terrestrial isotropic pyrite, with coherent values in peak position. Hematite was found in the alteration phase around pyrite grains as described by (Lorand et al., 2015) with peak value consistent throughout the breccia. McCubbin et al. (2016) obtained similar altered pyrite spectrum with a strong contribution of hematite. Pyrite with consistent Raman spectra has been observed in other Martian meteorites, such as shergottites (Wang et al., 2004a). Because the analytical total for the oxyhydroxide is 81% (Hewins et al., 2017), we speculate that it is a mixture of hematite and hydrated phases with a certain porosity.

5.3/ Bulk Raman spectra of the breccia

A SuperCam-like analysis was also performed. For this, a raw surface of the breccia was investigated using the TR Raman spectrometer in remote configuration with the telescope. In order to preserve the precious sample, the laser irradiance was set to a minimum value to observe peaks. Figure 17 shows a resulting Raman spectrum, raw and smoothed data, with some identifiable Raman peaks. A distinct peak doublet around $\sim 500 \text{ cm}^{-1}$ can be interpreted as feldspar. Given the low signal to noise ratio of the spectra, it is not possible to determine the composition of the feldspar accurately. An additional broad peak is visible at $\sim 665 \text{ cm}^{-1}$, likely due to an iron oxide like magnetite. Finally, a strong peak at $\sim 1010 \text{ cm}^{-1}$ is interpreted to reflect pyroxene. This spectrum thereby exhibits the three dominant minerals of the breccia which efficiently contribute to the average Raman spectra. Other frequent minerals, like phosphates, are not detected due to the sparse distribution of their grains. If the laser was precisely above a large grain, it would likely contribute to the overall spectra.

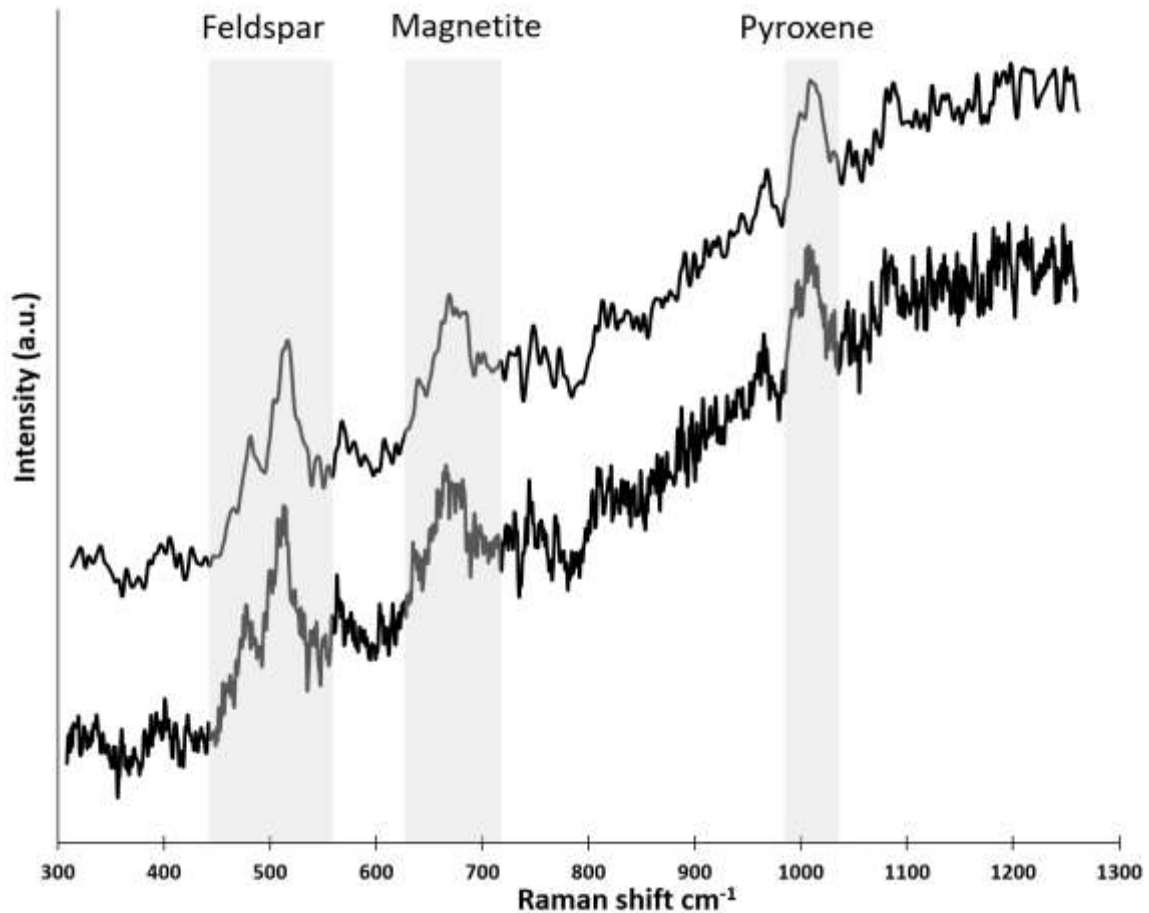


Fig. 17: Raw (bottom) and smoothed (top) spectra of a non-polished section performed with time-resolved Raman spectroscopy (gate 100 ns) in telescope mode and SuperCam-like conditions. The minerals contributing to the Raman spectra are highlighted above their distinct Raman peaks.

Conclusion

Raman spectroscopy is now on Mars on board Perseverance, and has already provided some key mineral identification that is not accessible directly to other techniques on the rover. Using Raman on Mars is challenging since the Raman signal is extremely weak and subtle. Laboratory studies on reference samples are therefore needed to help in optimizing analytical protocols on Mars, but also to deepen the spectral datasets to minerals that are likely to be found on Mars. This article provides for the first time an exhaustive Raman investigation of the regolith breccia NWA7533 which is one of the Martian meteorites offering the greatest mineralogical diversity. If the Raman signal is good enough, Raman on Mars could not only identify minerals but also provide some insight into their chemistry. We demonstrate also how luminescence could be used to detect and characterize trace elements (e.g. REE) in some key minerals like phosphates or zircon in Martian rocks.

References:

- Agee, C.B., Wilson, N.V., McCubbin, F.M., Ziegler, K., Polyak, V.J., Sharp, Z.D., Asmerom, Y., Nunn, M.H., Shaheen, R., Thiemens, M.H., Steele, A., Fogel, M.L., Bowden, R., Glamoclija, M., Zhang, Z., Elardo, S.M., 2013. Unique Meteorite from Early Amazonian Mars: Water-Rich Basaltic Breccia Northwest Africa 7034. *Science* 339, 780–785. <https://doi.org/10.1126/science.1228858>
- Befus, K.S., Lin, J.-F., Cisneros, M., Fu, S., 2018. Feldspar Raman shift and application as a magmatic thermobarometer. *Am. Mineral.* 103, 600–609. <https://doi.org/10.2138/am-2018-6157>
- Bellucci, J.J., Nemchin, A.A., Whitehouse, M.J., Humayun, M., Hewins, R., Zanda, B., 2015. Pb-isotopic evidence for an early, enriched crust on Mars. *Earth Planet. Sci. Lett.* 410, 34–41. <https://doi.org/10.1016/j.epsl.2014.11.018>
- Bernard, S., Beyssac, O., Benzerara, K., 2008. Raman Mapping Using Advanced Line-Scanning Systems: Geological Applications. *Appl. Spectrosc.* 62, 1180–1188. <https://doi.org/10.1366/000370208786401581>
- Bersani, D., Aliatis, I., Tribaudino, M., Mantovani, L., Benisek, A., Carpenter, M.A., Gatta, G.D., Lottici, P.P., 2018. Plagioclase composition by Raman spectroscopy. *J. Raman Spectrosc.* 49, 684–698. <https://doi.org/10.1002/jrs.5340>
- Beyssac, O., 2020. New Trends in Raman Spectroscopy: From High-Resolution Geochemistry to Planetary Exploration. *Elements* 16, 117–122. <https://doi.org/10.2138/gselements.16.2.117>
- Bhartia, R., Beegle, L.W., DeFlores, L., Abbey, W., Razzell Hollis, J., Uckert, K., Monacelli, B., Edgett, K.S., Kennedy, M.R., Sylvia, M., Aldrich, D., Anderson, M., Asher, S.A., Bailey, Z., Boyd, K., Burton, A.S., Caffrey, M., Calaway, M.J., Calvet, R., Cameron, B., Caplinger, M.A., Carrier, B.L., Chen, N., Chen, A., Clark, M.J., Clegg, S., Conrad, P.G., Cooper, M., Davis, K.N., Ehlmann, B., Facto, L., Fries, M.D., Garrison, D.H., Gasway, D., Ghaemi, F.T., Graff, T.G., Hand, K.P., Harris, C., Hein, J.D., Heinz, N., Herzog, H., Hochberg, E., Houck, A., Hug, W.F., Jensen, E.H., Kah, L.C., Kennedy, J., Krylo, R., Lam, J., Lindeman, M., McGlown, J., Michel, J., Miller, E., Mills, Z., Minitti, M.E., Mok, F., Moore, J., Nealon, K.H., Nelson, A., Newell, R., Nixon, B.E., Nordman, D.A., Nuding, D., Orellana, S., Pauken, M., Peterson, G., Pollock, R., Quinn, H., Quinto, C., Ravine, M.A., Reid, R.D., Riendeau, J., Ross, A.J., Sackos, J., Schaffner, J.A., Schwochert, M., O Shelton, M., Simon, R., Smith, C.L., Sobron, P., Steadman, K., Steele, A., Thiessen, D., Tran, V.D., Tsai, T., Tuite, M., Tung, E., Wehbe, R., Weinberg, R., Weiner, R.H., Wiens, R.C., Williford, K., Wollonciej, C., Wu, Y.-H., Yingst, R.A., Zan, J., 2021. Perseverance's Scanning Habitable Environments with Raman and Luminescence for Organics and Chemicals (SHERLOC) Investigation. *Space Sci. Rev.* 217, 58. <https://doi.org/10.1007/s11214-021-00812-z>
- Borg, L., 2005. A review of meteorite evidence for the timing of magmatism and of surface or near-surface liquid water on Mars. *J. Geophys. Res.* 110, E12S03. <https://doi.org/10.1029/2005JE002402>
- Carter, J., Poulet, F., 2013. Ancient plutonic processes on Mars inferred from the detection of possible anorthositic terrains. *Nat. Geosci.* 6, 1008–1012. <https://doi.org/10.1038/ngeo1995>
- Cartwright, J.A., Ott, U., Herrmann, S., Agee, C.B., 2014. Modern atmospheric signatures in 4.4 Ga Martian meteorite NWA 7034. *Earth Planet. Sci. Lett.* 400, 77–87. <https://doi.org/10.1016/j.epsl.2014.05.008>
- Černok, A., White, L.F., Darling, J., Dunlop, J., Anand, M., 2019. Shock-induced microtextures in lunar apatite and merrillite. *Meteorit. Planet. Sci.* 54, 1262–1282. <https://doi.org/10.1111/maps.13278>
- Cho, Y., Böttger, U., Rull, F., Hübers, H.-W., Belenguer, T., Börner, A., Buder, M., Bunduki, Y., Dietz, E., Hagelschuer, T., Kameda, S., Kopp, E., Lieder, M., Lopez-Reyes, G., Moral Inza, A.G., Mori, S., Ogura, J.A., Papproth, C., Perez Canora, C., Pertenais, M., Peter, G., Prieto-Ballesteros, O., Rockstein, S., Rodd-Routley, S., Rodriguez Perez, P., Ryan, C., Santamaria, P., Säuberlich, T., Schrandt, F., Schröder, S., Stangarone, C., Ulamec, S., Usui, T., Weber, I., Westerdorff, K., Yumoto, K., 2021. In situ science on Phobos with the Raman spectrometer for MMX (RAX): preliminary design and feasibility of Raman measurements. *Earth Planets Space* 73, 232. <https://doi.org/10.1186/s40623-021-01496-z>
- Christensen, P.R., Bandfield, J.L., Hamilton, V.E., Ruff, S.W., Kieffer, H.H., Titus, T.N., Malin, M.C., Morris, R.V., Lane, M.D., Clark, R.L., Jakosky, B.M., Mellon, M.T., Pearl, J.C.,

- Conrath, B.J., Smith, M.D., Clancy, R.T., Kuzmin, R.O., Roush, T., Mehall, G.L., Gorelick, N., Bender, K., Murray, K., Dason, S., Greene, E., Silverman, S., Greenfield, M., 2001. Mars Global Surveyor Thermal Emission Spectrometer experiment: Investigation description and surface science results. *J. Geophys. Res. Planets* 106, 23823–23871. <https://doi.org/10.1029/2000JE001370>
- Christensen, P.R., Jakosky, B.M., Kieffer, H.H., Malin, M.C., Mewsween, H.Y., Neelson, K., Mehall, G.L., Silverman, S.H., Ferry, S., Caplinger, M., Ravine, M., 2002. THE THERMAL EMISSION IMAGING SYSTEM (THEMIS) FOR THE MARS 2001 ODYSSEY MISSION.
- Cooney, T.F., Scott, E.R.D., Krot, A.N., Sharma, S.K., Yamaguchi, A., 1999. Vibrational spectroscopic study of minerals in the Martian meteorite ALH 84001. *Am. Mineral.* 84, 1569–1576. <https://doi.org/10.2138/am-1999-1010>
- Cousin, A., Sautter, V., Payré, V., Forni, O., Mangold, N., Gasnault, O., Le Deit, L., Johnson, J., Maurice, S., Salvatore, M., Wiens, R.C., Gasda, P., Rapin, W., 2017. Classification of igneous rocks analyzed by ChemCam at Gale crater, Mars. *Icarus* 288, 265–283. <https://doi.org/10.1016/j.icarus.2017.01.014>
- Cox, M.A., Cavosie, A.J., Orr, K.J., Daly, L., Martin, L., Lagain, A., Benedix, G.K., Bland, P.A., 2022. Impact and habitability scenarios for early Mars revisited based on a 4.45-Ga shocked zircon in regolith breccia. *Sci. Adv.* 8, eabl7497. <https://doi.org/10.1126/sciadv.abl7497>
- Dawson, P., Hargreave, M.M., Wilkinson, G.R., 1971. The vibrational spectrum of zircon (zrsio₄). *J. Phys. C Solid State Phys.* 4, 240–256. <https://doi.org/10.1088/0022-3719/4/2/014>
- Dyar, M.D., Tucker, J.M., Humphries, S., Clegg, S.M., Wiens, R.C., Lane, M.D., 2011. Strategies for Mars remote Laser-Induced Breakdown Spectroscopy analysis of sulfur in geological samples. *Spectrochim. Acta Part B At. Spectrosc.* 66, 39–56. <https://doi.org/10.1016/j.sab.2010.11.016>
- Farley, K.A., Stack, K.M., Shuster, D.L., Horgan, B.H.N., Hurowitz, J.A., Tarnas, J.D., Simon, J.I., Sun, V.Z., Scheller, E.L., Moore, K.R., McLennan, S.M., Vasconcelos, P.M., Wiens, R.C., Treiman, A.H., Mayhew, L.E., Beyssac, O., Kizovski, T.V., Tosca, N.J., Williford, K.H., Crumpler, L.S., Beegle, L.W., Bell, J.F., Ehlmann, B.L., Liu, Y., Maki, J.N., Schmidt, M.E., Allwood, A.C., Amundsen, H.E.F., Bhartia, R., Bosak, T., Brown, A.J., Clark, B.C., Cousin, A., Forni, O., Gabriel, T.S.J., Goreva, Y., Gupta, S., Hamran, S.-E., Herd, C.D.K., Hickman-Lewis, K., Johnson, J.R., Kah, L.C., Kelemen, P.B., Kinch, K.B., Mandon, L., Mangold, N., Quantin-Nataf, C., Rice, M.S., Russell, P.S., Sharma, S., Siljeström, S., Steele, A., Sullivan, R., Wadhwa, M., Weiss, B.P., Williams, A.J., Wogsland, B.V., Willis, P.A., Acosta-Maeda, T.A., Beck, P., Benzerara, K., Bernard, S., Burton, A.S., Cardarelli, E.L., Chide, B., Clavé, E., Cloutis, E.A., Cohen, B.A., Czajka, A.D., Debaille, V., Dehouck, E., Fairén, A.G., Flannery, D.T., Fleron, S.Z., Fouchet, T., Frydenvang, J., Garczynski, B.J., Gibbons, E.F., Hausrath, E.M., Hayes, A.G., Henneke, J., Jørgensen, J.L., Kelly, E.M., Lasue, J., Le Mouélic, S., Madariaga, J.M., Maurice, S., Merusi, M., Meslin, P.-Y., Milkovich, S.M., Million, C.C., Moeller, R.C., Núñez, J.I., Ollila, A.M., Paar, G., Paige, D.A., Pedersen, D.A.K., Pilleri, P., Pilorget, C., Pinet, P.C., Rice, J.W., Royer, C., Sautter, V., Schulte, M., Sephton, M.A., Sharma, S.K., Sholes, S.F., Spanovich, N., St. Clair, M., Tate, C.D., Uckert, K., VanBommel, S.J., Yanchilina, A.G., Zorzano, M.-P., 2022. Aqueously altered igneous rocks sampled on the floor of Jezero crater, Mars. *Science* 377, eabo2196. <https://doi.org/10.1126/science.abo2196>
- Fau, A., Beyssac, O., Gauthier, M., Meslin, P.Y., Cousin, A., Benzerara, K., Bernard, S., Boulliard, J.C., Gasnault, O., Forni, O., Wiens, R.C., Morand, M., Rosier, P., Garino, Y., Pont, S., Maurice, S., 2019. Pulsed laser-induced heating of mineral phases: Implications for laser-induced breakdown spectroscopy combined with Raman spectroscopy. *Spectrochim. Acta Part B At. Spectrosc.* 160, 105687. <https://doi.org/10.1016/j.sab.2019.105687>
- Fau, A., Beyssac, O., Gauthier, M., Panczer, G., Gasnault, O., Meslin, P.-Y., Bernard, S., Maurice, S., Forni, O., Boulliard, J.-C., Bosc, F., Drouet, C., 2022. Time-resolved Raman and luminescence spectroscopy of synthetic REE-doped hydroxylapatites and natural apatites. *Am. Mineral.* 107, 1341–1352. <https://doi.org/10.2138/am-2022-8006>
- Franz, H.B., Kim, S.-T., Farquhar, J., Day, J.M.D., Economos, R.C., McKeegan, K.D., Schmitt, A.K., Irving, A.J., Hoek, J., Dottin, J., 2014. Isotopic links between atmospheric chemistry and the deep sulphur cycle on Mars. *Nature* 508, 364–368. <https://doi.org/10.1038/nature13175>

- Freeman, J.J., Wang, A., Kuebler, K.E., Jolliff, B.L., Haskin, L.A., 2008. CHARACTERIZATION OF NATURAL FELDSPARS BY RAMAN SPECTROSCOPY FOR FUTURE PLANETARY EXPLORATION. *Can. Mineral.* 46, 1477–1500. <https://doi.org/10.3749/canmin.46.6.1477>
- Frezzotti, M.L., Tecce, F., Casagli, A., 2012. Raman spectroscopy for fluid inclusion analysis. *J. Geochim. Explor.* 112, 1–20. <https://doi.org/10.1016/j.gexplo.2011.09.009>
- Gaft, M., Reisfeld, R., Panczer, G., 2015. *Modern Luminescence Spectroscopy of Minerals and Materials*, Springer Mineralogy. Springer International Publishing, Cham. <https://doi.org/10.1007/978-3-319-24765-6>
- Gattacceca, J., Rochette, P., Scorzelli, R.B., Munayco, P., Agee, C., Quesnel, Y., Cournède, C., Geissman, J., 2014. Martian meteorites and Martian magnetic anomalies: A new perspective from NWA 7034: Martian meteorites & magnetic anomalies. *Geophys. Res. Lett.* 41, 4859–4864. <https://doi.org/10.1002/2014GL060464>
- Hewins, R.H., Zanda, B., Humayun, M., Nemchin, A., Lorand, J.-P., Pont, S., Deldicque, D., Bellucci, J.J., Beck, P., Leroux, H., Marinova, M., Remusat, L., Göpel, C., Lewin, E., Grange, M., Kennedy, A., Whitehouse, M.J., 2017. Regolith breccia Northwest Africa 7533: Mineralogy and petrology with implications for early Mars. *Meteorit. Planet. Sci.* 52, 89–124. <https://doi.org/10.1111/maps.12740>
- Hoefen, T.M., Clark, R.N., Bandfield, J.L., Smith, M.D., Pearl, J.C., Christensen, P.R., 2003. Discovery of Olivine in the Nili Fossae Region of Mars. *Science* 302, 627–630. <https://doi.org/10.1126/science.1089647>
- Hu, S., Lin, Y., Zhang, J., Hao, J., Xing, W., Zhang, T., Yang, W., Changela, H., 2019. Ancient geologic events on Mars revealed by zircons and apatites from the Martian regolith breccia NWA 7034. *Meteorit. Planet. Sci.* 54, 850–879. <https://doi.org/10.1111/maps.13256>
- Huang, E., Chen, C.H., Huang, T., Lin, E.H., Xu, J., 2000. Raman spectroscopic characteristics of Mg-Fe-Ca pyroxenes. *Am. Mineral.* 85, 473–479. <https://doi.org/10.2138/am-2000-0408>
- Humayun, M., Nemchin, A., Zanda, B., Hewins, R.H., Grange, M., Kennedy, A., Lorand, J.-P., Göpel, C., Fieni, C., Pont, S., Deldicque, D., 2013. Origin and age of the earliest Martian crust from meteorite NWA 7533. *Nature* 503, 513–516. <https://doi.org/10.1038/nature12764>
- Jia, M., Zhai, K., Gao, M., Wen, W., Liu, Y., Wu, X., Zhai, S., 2020. Raman spectra and X-ray diffraction of merrillite at various temperatures. *Vib. Spectrosc.* 106, 103005. <https://doi.org/10.1016/j.vibspec.2019.103005>
- Jolliff, B.L., Hughes, J.M., Freeman, J.J., Zeigler, R.A., 2006. Crystal chemistry of lunar merrillite and comparison to other meteoritic and planetary suites of whitlockite and merrillite. *Am. Mineral.* 91, 1583–1595. <https://doi.org/10.2138/am.2006.2185>
- Kuebler, K.E., Jolliff, B.L., Wang, A., Haskin, L.A., 2006. Extracting olivine (Fo–Fa) compositions from Raman spectral peak positions. *Geochim. Cosmochim. Acta* 70, 6201–6222. <https://doi.org/10.1016/j.gca.2006.07.035>
- Leroux, H., Jacob, D., Marinova, M., Hewins, R.H., Zanda, B., Pont, S., Lorand, J., Humayun, M., 2016. Exsolution and shock microstructures of igneous pyroxene clasts in the Northwest Africa 7533 Martian meteorite. *Meteorit. Planet. Sci.* 51, 932–945. <https://doi.org/10.1111/maps.12637>
- Litasov, K.D., Podgornykh, N.M., 2017. Raman spectroscopy of various phosphate minerals and occurrence of tuite in the Elga IIE iron meteorite: Raman spectroscopy of various phosphate minerals. *J. Raman Spectrosc.* 48, 1518–1527. <https://doi.org/10.1002/jrs.5119>
- Liu, Y., Tice, M.M., Schmidt, M.E., Treiman, A.H., Kizovski, T.V., Hurowitz, J.A., Allwood, A.C., Henneke, J., Pedersen, D.A.K., VanBommel, S.J., Jones, M.W.M., Knight, A.L., Orenstein, B.J., Clark, B.C., Elam, W.T., Heirwegh, C.M., Barber, T., Beegle, L.W., Benzerara, K., Bernard, S., Beyssac, O., Bosak, T., Brown, A.J., Cardarelli, E.L., Catling, D.C., Christian, J.R., Cloutis, E.A., Cohen, B.A., Davidoff, S., Fairén, A.G., Farley, K.A., Flannery, D.T., Galvin, A., Grotzinger, J.P., Gupta, S., Hall, J., Herd, C.D.K., Hickman-Lewis, K., Hodyss, R.P., Horgan, B.H.N., Johnson, J.R., Jørgensen, J.L., Kah, L.C., Maki, J.N., Mandon, L., Mangold, N., McCubbin, F.M., McLennan, S.M., Moore, K., Nachon, M., Nemere, P., Nothdurft, L.D., Núñez, J.I., O’Neil, L., Quantin-Nataf, C.M., Sautter, V., Shuster, D.L., Siebach, K.L., Simon, J.I., Sinclair, K.P., Stack, K.M., Steele, A., Tarnas, J.D., Tosca, N.J., Uckert, K., Udry, A., Wade, L.A., Weiss, B.P., Wiens, R.C., Williford, K.H., Zorzano, M.-P.,

2022. An olivine cumulate outcrop on the floor of Jezero crater, Mars. *Science* 377, 1513–1519. <https://doi.org/10.1126/science.abo2756>
- Lorand, J.-P., Hewins, R.H., Humayun, M., Remusat, L., Zanda, B., La, C., Pont, S., 2018. Chalcophile-siderophile element systematics of hydrothermal pyrite from martian regolith breccia NWA 7533. *Geochim. Cosmochim. Acta* 241, 134–149. <https://doi.org/10.1016/j.gca.2018.08.041>
- Lorand, J.-P., Hewins, R.H., Remusat, L., Zanda, B., Pont, S., Leroux, H., Marinova, M., Jacob, D., Humayun, M., Nemchin, A., Grange, M., Kennedy, A., Göpel, C., 2015. Nickeliferous pyrite tracks pervasive hydrothermal alteration in Martian regolith breccia: A study in NWA 7533. *Meteorit. Planet. Sci.* 50, 2099–2120. <https://doi.org/10.1111/maps.12565>
- Maurice, S., Wiens, R.C., Bernardi, P., Caïs, P., Robinson, S., Nelson, T., Gasnault, O., Reess, J.-M., Deleuze, M., Rull, F., Manrique, J.-A., Abbaki, S., Anderson, R.B., André, Y., Angel, S.M., Arana, G., Battault, T., Beck, P., Benzerara, K., Bernard, S., Berthias, J.-P., Beyssac, O., Bonafous, M., Bousquet, B., Boutillier, M., Cadu, A., Castro, K., Chapron, F., Chide, B., Clark, K., Clavé, E., Clegg, S., Cloutis, E., Collin, C., Cordoba, E.C., Cousin, A., Dameury, J.-C., D'Anna, W., Daydou, Y., Debus, A., Deflores, L., Dehouck, E., Delapp, D., De Los Santos, G., Donny, C., Doressoundiram, A., Dromart, G., Dubois, B., Dufour, A., Dupieux, M., Egan, M., Ervin, J., Fabre, C., Fau, A., Fischer, W., Forni, O., Fouchet, T., Frydenvang, J., Gauffre, S., Gauthier, M., Gharakanian, V., Gilard, O., Gontijo, I., Gonzalez, R., Granena, D., Grotzinger, J., Hassen-Khodja, R., Heim, M., Hello, Y., Hervet, G., Humeau, O., Jacob, X., Jacquino, S., Johnson, J.R., Kouach, D., Lacombe, G., Lanza, N., Lapauw, L., Laserna, J., Lasue, J., Le Deit, L., Le Mouélic, S., Le Comte, E., Lee, Q.-M., Legett, C., Leveille, R., Lewin, E., Leyrat, C., Lopez-Reyes, G., Lorenz, R., Lucero, B., Madariaga, J.M., Madsen, S., Madsen, M., Mangold, N., Manni, F., Mariscal, J.-F., Martinez-Frias, J., Mathieu, K., Mathon, R., McCabe, K.P., McConnochie, T., McLennan, S.M., Mekki, J., Melikechi, N., Meslin, P.-Y., Micheau, Y., Michel, Y., Michel, J.M., Mimoun, D., Misra, A., Montagnac, G., Montaron, C., Montmessin, F., Moros, J., Mousset, V., Morizet, Y., Murdoch, N., Newell, R.T., Newsom, H., Nguyen Tuong, N., Ollila, A.M., Orttner, G., Oudda, L., Pares, L., Parisot, J., Parot, Y., Pérez, R., Pheav, D., Picot, L., Pilleri, P., Pilorget, C., Pinet, P., Pont, G., Poulet, F., Quantin-Nataf, C., Quertier, B., Rambaud, D., Rapin, W., Romano, P., Roucayrol, L., Royer, C., Ruellan, M., Sandoval, B.F., Sautter, V., Schoppers, M.J., Schröder, S., Seran, H.-C., Sharma, S.K., Sobron, P., Sodki, M., Sournac, A., Sridhar, V., Standarovskiy, D., Storms, S., Striebig, N., Tatat, M., Toplis, M., Torre-Fdez, I., Toulemon, N., Velasco, C., Veneranda, M., Venhaus, D., Virmontois, C., Viso, M., Willis, P., Wong, K.W., 2021. The SuperCam Instrument Suite on the Mars 2020 Rover: Science Objectives and Mast-Unit Description. *Space Sci. Rev.* 217, 47. <https://doi.org/10.1007/s11214-021-00807-w>
- McCubbin, F.M., Boyce, J.W., Novák-Szabó, T., Santos, A.R., Tartèse, R., Muttik, N., Domokos, G., Vazquez, J., Keller, L.P., Moser, D.E., Jerolmack, D.J., Shearer, C.K., Steele, A., Elardo, S.M., Rahman, Z., Anand, M., Delhaye, T., Agee, C.B., 2016. Geologic history of Martian regolith breccia Northwest Africa 7034: Evidence for hydrothermal activity and lithologic diversity in the Martian crust: Geologic History of NWA 7034. *J. Geophys. Res. Planets* 121, 2120–2149. <https://doi.org/10.1002/2016JE005143>
- McSween, H.Y., Ruff, S.W., Morris, R.V., Gellert, R., Klingelhöfer, G., Christensen, P.R., McCoy, T.J., Ghosh, A., Moersch, J.M., Cohen, B.A., Rogers, A.D., Schröder, C., Squyres, S.W., Crisp, J., Yen, A., 2008. Mineralogy of volcanic rocks in Gusev Crater, Mars: Reconciling Mössbauer, Alpha Particle X-Ray Spectrometer, and Miniature Thermal Emission Spectrometer spectra. *J. Geophys. Res.* 113, E06S04. <https://doi.org/10.1029/2007JE002970>
- Megevand, V., Viennet, J.C., Balan, E., Gauthier, M., Rosier, P., Morand, M., Garino, Y., Guillaumet, M., Pont, S., Beyssac, O., Bernard, S., 2021. Impact of UV Radiation on the Raman Signal of Cystine: Implications for the Detection of S-rich Organics on Mars. *Astrobiology* 21, 566–574. <https://doi.org/10.1089/ast.2020.2340>
- Mernagh, T.P., 1991. Use of the laser Raman microprobe for discrimination amongst feldspar minerals. *J. Raman Spectrosc.* 22, 453–457. <https://doi.org/10.1002/jrs.1250220806>
- Mernagh, T.P., Trudu, A.G., 1993. A laser Raman microprobe study of some geologically important sulphide minerals. *Chem. Geol.* 103, 113–127. [https://doi.org/10.1016/0009-2541\(93\)90295-T](https://doi.org/10.1016/0009-2541(93)90295-T)

- Mikouchi, T., Miyamoto, M., 2000. Micro Raman spectroscopy of amphiboles and pyroxenes in the martian meteorites Zagami and Lewis Cliff 88516. *Meteorit. Planet. Sci.* 35, 155–159. <https://doi.org/10.1111/j.1945-5100.2000.tb01982.x>
- Mustard, J.F., Poulet, F., Gendrin, A., Bibring, J.-P., Langevin, Y., Gondet, B., Mangold, N., Bellucci, G., Altieri, F., 2005. Olivine and Pyroxene Diversity in the Crust of Mars. *Science* 307, 1594–1597. <https://doi.org/10.1126/science.1109098>
- Nasdala, L., Irmer, G., Jonckheere, R., 2002. Radiation damage ages: Practical concept or impractical vision? – Reply to two comments on ““Metamictisation of natural zircon: Accumulation versus thermal annealing of radioactivity-induced damage””, and further discussion.
- Nasdala, L., Wenzel, M., Vavra, G., Irmer, G., Wenzel, T., Kober, B., 2001. Metamictisation of natural zircon: accumulation versus thermal annealing of radioactivity-induced damage. *Contrib. Mineral. Petrol.* 141, 125–144. <https://doi.org/10.1007/s004100000235>
- Ody, A., Poulet, F., Bibring, J.-P., Loizeau, D., Carter, J., Gondet, B., Langevin, Y., 2013. Global investigation of olivine on Mars: Insights into crust and mantle compositions: GLOBAL INVESTIGATION OF OLIVINE ON MARS. *J. Geophys. Res. Planets* 118, 234–262. <https://doi.org/10.1029/2012JE004149>
- Papike, J.J., Karner, J.M., Shearer, C.K., Burger, P.V., 2009. Silicate mineralogy of martian meteorites. *Geochim. Cosmochim. Acta* 73, 7443–7485. <https://doi.org/10.1016/j.gca.2009.09.008>
- Pasteris, J.D., Beyssac, O., 2020. Welcome to Raman Spectroscopy: Successes, Challenges, and Pitfalls. *Elements* 16, 87–92. <https://doi.org/10.2138/gselements.16.2.87>
- Peck, W.H., Valley, J.W., Wilde, S.A., Graham, C.M., 2001. Oxygen isotope ratios and rare earth elements in 3.3 to 4.4 Ga zircons: Ion microprobe evidence for high $\delta^{18}\text{O}$ continental crust and oceans in the Early Archean.
- Pellas, P., 1954. Sur la formation de l'état métamictite dans le zircon. *Bull. Société Fr. Minéralogie Cristallogr.* 77, 447–460. <https://doi.org/10.3406/bulmi.1954.4899>
- Rogers, A.D., Nekvasil, H., 2015. Feldspathic rocks on Mars: Compositional constraints from infrared spectroscopy and possible formation mechanisms: Feldspathic rocks on Mars: constraints. *Geophys. Res. Lett.* 42, 2619–2626. <https://doi.org/10.1002/2015GL063501>
- Roszjar, J., Moser, D.E., Hyde, B.C., Chanmuang, C., Tait, K., 2017. Comparing Chemical Microstructures of Some Early Solar System Zircon from Differentiated Asteroids, Mars and Earth, in: Moser, D.E., Corfu, F., Darling, J.R., Reddy, S.M., Tait, K. (Eds.), *Geophysical Monograph Series*. John Wiley & Sons, Inc., Hoboken, NJ, USA, pp. 113–135. <https://doi.org/10.1002/9781119227250.ch5>
- Rull, F., Martínez-Frias, J., Rodríguez-Losada, J.A., 2007. Micro-Raman spectroscopic study of El Gasco pumice, western Spain. *J. Raman Spectrosc.* 38, 239–244. <https://doi.org/10.1002/jrs.1628>
- Rull, F., Martínez-Frias, J., Sansano, A., Medina, J., Edwards, H.G.M., 2004. Comparative micro-Raman study of the Nakhla and Vaca Muerta meteorites. *J. Raman Spectrosc.* 35, 497–503. <https://doi.org/10.1002/jrs.1177>
- Rull, F., Maurice, S., Hutchinson, I., Moral, A., Perez, C., Diaz, C., Colombo, M., Belenguer, T., Lopez-Reyes, G., Sansano, A., Forni, O., Parot, Y., Striebig, N., Woodward, S., Howe, C., Tarcea, N., Rodriguez, P., Seoane, L., Santiago, A., Rodriguez-Prieto, J.A., Medina, J., Gallego, P., Canchal, R., Santamaría, P., Ramos, G., Vago, J.L., on behalf of the RLS Team, 2017. The Raman Laser Spectrometer for the ExoMars Rover Mission to Mars. *Astrobiology* 17, 627–654. <https://doi.org/10.1089/ast.2016.1567>
- Santos, A.R., Agee, C.B., McCubbin, F.M., Shearer, C.K., Burger, P.V., Tartèse, R., Anand, M., 2015. Petrology of igneous clasts in Northwest Africa 7034: Implications for the petrologic diversity of the martian crust. *Geochim. Cosmochim. Acta* 157, 56–85. <https://doi.org/10.1016/j.gca.2015.02.023>
- Sautter, V., Toplis, M.J., Wiens, R.C., Cousin, A., Fabre, C., Gasnault, O., Maurice, S., Forni, O., Lasue, J., Ollila, A., Bridges, J.C., Mangold, N., Le Mouélic, S., Fisk, M., Meslin, P.-Y., Beck, P., Pinet, P., Le Deit, L., Rapin, W., Stolper, E.M., Newsom, H., Dyar, D., Lanza, N.,

- Vaniman, D., Clegg, S., Wray, J.J., 2015. In situ evidence for continental crust on early Mars. *Nat. Geosci.* 8, 605–609. <https://doi.org/10.1038/ngeo2474>
- Scheller, E.L., Razzell Hollis, J., Cardarelli, E.L., Steele, A., Beegle, L.W., Bhartia, R., Conrad, P., Uckert, K., Sharma, S., Ehlmann, B.L., Abbey, W.J., Asher, S.A., Benison, K.C., Berger, E.L., Beyssac, O., Bleefeld, B.L., Bosak, T., Brown, A.J., Burton, A.S., Bykov, S.V., Cloutis, E., Fairén, A.G., DeFlores, L., Farley, K.A., Fey, D.M., Fornaro, T., Fox, A.C., Fries, M., Hickman-Lewis, K., Hug, W.F., Huggett, J.E., Imbeah, S., Jakubek, R.S., Kah, L.C., Kelemen, P., Kennedy, M.R., Kizovski, T., Lee, C., Liu, Y., Mandon, L., McCubbin, F.M., Moore, K.R., Nixon, B.E., Núñez, J.I., Rodriguez Sanchez-Vahamonde, C., Roppel, R.D., Schulte, M., Sephton, M.A., Sharma, S.K., Siljeström, S., Shkolyar, S., Shuster, D.L., Simon, J.I., Smith, R.J., Stack, K.M., Steadman, K., Weiss, B.P., Werynski, A., Williams, A.J., Wiens, R.C., Williford, K.H., Winchell, K., Wogsland, B., Yanchilina, A., Yingling, R., Zorzano, M.-P., 2022. Aqueous alteration processes in Jezero crater, Mars—implications for organic geochemistry. *Science* 378, 1105–1110. <https://doi.org/10.1126/science.abo5204>
- Shebanova, O.N., Lazor, P., 2003. Raman spectroscopic study of magnetite (FeFe₂O₄): a new assignment for the vibrational spectrum. *J. Solid State Chem.* 174, 424–430. [https://doi.org/10.1016/S0022-4596\(03\)00294-9](https://doi.org/10.1016/S0022-4596(03)00294-9)
- Smith, A., Hallis, L.J., Nagashima, K., Huss, G.R., 2020. Volatile abundances and hydrogen isotope ratios of apatite in Martian basaltic breccia NWA 11522—A paired stone of NWA 7034. *Meteorit. Planet. Sci.* 55, 2587–2598. <https://doi.org/10.1111/maps.13605>
- Syme, R.W.G., Lockwood, D.J., Kerr, H.J., 1977. Raman spectrum of synthetic zircon (ZrSiO₄) and thorite (ThSiO₄). *J. Phys. C Solid State Phys.* 10, 1335–1348. <https://doi.org/10.1088/0022-3719/10/8/036>
- Udry, A., Howarth, G.H., Herd, C.D.K., Day, J.M.D., Lapen, T.J., Filiberto, J., 2020. What Martian Meteorites Reveal About the Interior and Surface of Mars. *J. Geophys. Res. Planets* 125. <https://doi.org/10.1029/2020JE006523>
- Udry, A., Lunning, N.G., McSween, H.Y., Bodnar, R.J., 2014. Petrogenesis of a vitrophyre in the martian meteorite breccia NWA 7034. *Geochim. Cosmochim. Acta* 141, 281–293. <https://doi.org/10.1016/j.gca.2014.06.026>
- Váczí, T., 2014. A New, Simple Approximation for the Deconvolution of Instrumental Broadening in Spectroscopic Band Profiles. *Appl. Spectrosc.* 68, 1274–1278. <https://doi.org/10.1366/13-07275>
- Wang, A., Jolliff, B.L., Haskin, L.A., 1999. Raman spectroscopic characterization of a Martian SNC meteorite: Zagami. *J. Geophys. Res. Planets* 104, 8509–8519. <https://doi.org/10.1029/1999JE900004>
- Wang, A., Jolliff, B.L., Haskin, L.A., Kuebler, K.E., Viskupic, K.M., 2001. Characterization and comparison of structural and compositional features of planetary quadrilateral pyroxenes by Raman spectroscopy. *Am. Mineral.* 86, 790–806. <https://doi.org/10.2138/am-2001-0703>
- Wang, A., Jolliff, B.L., Viskupic, K.M., Haskin, L.A., 1997. RAMAN SPECTROSCOPIC CHARACTERIZATION OF DIFFERENT TYPES OF.
- Wang, A., Kuebler, K., Jolliff, B., Haskin, L.A., 2004a. Mineralogy of a Martian meteorite as determined by Raman spectroscopy. *J. Raman Spectrosc.* 35, 504–514. <https://doi.org/10.1002/jrs.1175>
- Wang, A., Kuebler, K.E., Jolliff, B.L., Haskin, L.A., 2004b. Raman spectroscopy of Fe-Ti-Cr-oxides, case study: Martian meteorite EETA79001. *Am. Mineral.* 89, 665–680. <https://doi.org/10.2138/am-2004-5-601>
- Weber, I., Böttger, U., Pavlov, S.G., Jessberger, E.K., Hübers, H.-W., 2014. Mineralogical and Raman spectroscopy studies of natural olivines exposed to different planetary environments. *Planet. Space Sci.* 104, 163–172. <https://doi.org/10.1016/j.pss.2014.08.016>
- Wiens, R.C., Maurice, S., Robinson, S.H., Nelson, A.E., Cais, P., Bernardi, P., Newell, R.T., Clegg, S., Sharma, S.K., Storms, S., Deming, J., Beckman, D., Ollila, A.M., Gasnault, O., Anderson, R.B., André, Y., Michael Angel, S., Arana, G., Auden, E., Beck, P., Becker, J., Benzerara, K., Bernard, S., Beyssac, O., Borges, L., Bousquet, B., Boyd, K., Caffrey, M., Carlson, J., Castro, K., Celis, J., Chide, B., Clark, K., Cloutis, E., Cordoba, E.C., Cousin, A., Dale, M., Deflores, L., Delapp, D., Deleuze, M., Dirmyer, M., Donny, C., Dromart, G., George Duran, M., Egan,

- M., Ervin, J., Fabre, C., Fau, A., Fischer, W., Forni, O., Fouchet, T., Fresquez, R., Frydenvang, J., Gasway, D., Gontijo, I., Grotzinger, J., Jacob, X., Jacquino, S., Johnson, J.R., Klisiewicz, R.A., Lake, J., Lanza, N., Laserna, J., Lasue, J., Le Mouélic, S., Legett, C., Leveille, R., Lewin, E., Lopez-Reyes, G., Lorenz, R., Lorigny, E., Love, S.P., Lucero, B., Madariaga, J.M., Madsen, M., Madsen, S., Mangold, N., Manrique, J.A., Martinez, J.P., Martinez-Frias, J., McCabe, K.P., McConnochie, T.H., McGlown, J.M., McLennan, S.M., Melikechi, N., Meslin, P.-Y., Michel, J.M., Mimoun, D., Misra, A., Montagnac, G., Montmessin, F., Mousset, V., Murdoch, N., Newsom, H., Ott, L.A., Ousnamer, Z.R., Pares, L., Parot, Y., Pawluczyk, R., Glen Peterson, C., Pilleri, P., Pinet, P., Pont, G., Poulet, F., Provost, C., Quartier, B., Quinn, H., Rapin, W., Reess, J.-M., Regan, A.H., Reyes-Newell, A.L., Romano, P.J., Royer, C., Rull, F., Sandoval, B., Sarrao, J.H., Sautter, V., Schoppers, M.J., Schröder, S., Seitz, D., Shepherd, T., Sobron, P., Dubois, B., Sridhar, V., Toplis, M.J., Torre-Fdez, I., Trettel, I.A., Underwood, M., Valdez, A., Valdez, J., Venhaus, D., Willis, P., 2021. The SuperCam Instrument Suite on the NASA Mars 2020 Rover: Body Unit and Combined System Tests. *Space Sci. Rev.* 217, 4. <https://doi.org/10.1007/s11214-020-00777-5>
- Wiens, R.C., Udry, A., Beyssac, O., Quantin-Nataf, C., Mangold, N., Cousin, A., Mandon, L., Bosak, T., Forni, O., McLennan, S.M., Sautter, V., Brown, A., Benzerara, K., Johnson, J.R., Mayhew, L., Maurice, S., Anderson, R.B., Clegg, S.M., Crumpler, L., Gabriel, T.S.J., Gasda, P., Hall, J., Horgan, B.H.N., Kah, L., Legett, C., Madariaga, J.M., Meslin, P.-Y., Ollila, A.M., Poulet, F., Royer, C., Sharma, S.K., Siljeström, S., Simon, J.I., Acosta-Maeda, T.E., Alvarez-Llamas, C., Angel, S.M., Arana, G., Beck, P., Bernard, S., Bertrand, T., Bousquet, B., Castro, K., Chide, B., Clavé, E., Cloutis, E., Connell, S., Dehouck, E., Dromart, G., Fischer, W., Fouchet, T., Francis, R., Frydenvang, J., Gasnault, O., Gibbons, E., Gupta, S., Hausrath, E.M., Jacob, X., Kalucha, H., Kelly, E., Knutsen, E., Lanza, N., Laserna, J., Lasue, J., Le Mouélic, S., Leveille, R., Lopez Reyes, G., Lorenz, R., Manrique, J.A., Martinez-Frias, J., McConnochie, T., Melikechi, N., Mimoun, D., Montmessin, F., Moros, J., Murdoch, N., Pilleri, P., Pilorget, C., Pinet, P., Rapin, W., Rull, F., Schröder, S., Shuster, D.L., Smith, R.J., Stott, A.E., Tarnas, J., Turenne, N., Veneranda, M., Vogt, D.S., Weiss, B.P., Willis, P., Stack, K.M., Williford, K.H., Farley, K.A., The SuperCam Team, 2022. Compositionally and density stratified igneous terrain in Jezero crater, Mars. *Mars. Sci. Adv.* 8, eabo3399. <https://doi.org/10.1126/sciadv.abo3399>
- Wilde, S.A., Valley, J.W., Peck, W.H., Graham, C.M., 2001. Evidence from detrital zircons for the existence of continental crust and oceans on the Earth 4.4 Gyr ago. *Nature* 409, 175–178. <https://doi.org/10.1038/35051550>
- Wittmann, A., Korotev, R.L., Jolliff, B.L., Irving, A.J., Moser, D.E., Barker, I., Rumble, D., 2015. Petrography and composition of Martian regolith breccia meteorite Northwest Africa 7475. *Meteorit. Planet. Sci.* 50, 326–352. <https://doi.org/10.1111/maps.12425>
- Zhang, B., Shieh, S.R., Withers, A.C., Bouvier, A., 2018. Raman spectroscopy of shocked enstatite-rich meteorites. *Meteorit. Planet. Sci.* 53, 2067–2077. <https://doi.org/10.1111/maps.13106>

Kuebler, K., Wang, J.J., Jolliff, B.L., 2006b. Database of Raman mineral spectra for planetary surface exploration. LPSC XXXVII, abs 1907.

Jolliff, B.L., Freeman, J.J., Wopenka, W., 1996. Structural comparison of lunar, terrestrial and synthetic whitlockite using laser Raman microprobe spectroscopy. LPSC XXVII, abs 613.

Imae, N., Ikeda, Y., 2010. High-pressure polymorphs of magnesian orthopyroxene from a shock vein in the Yamato-000047 lherzolitic shergottite.

Fritz, J., Greshake, A., Stöffler, D., 2005. Micro-Raman spectroscopy of plagioclase and maskelynite in Martian meteorites: Evidence of progressive shock metamorphism. *Antarct. Meteorite. Res.*, 18, 96–116.

O'Shea, D.C., Bartlett, M.L., Young, R.A., 1974. Compositional analysis of apatites with Laser-Raman spectroscopy: (OH, F, Cl) apatites. *Arch. Oral. Biol.* Vol. 19. pp. 995 to 1006.